

A Tensor Decomposition-Based Anomaly Detection Algorithm for Hyperspectral Image

Xing Zhang, Gongjian Wen, *Member, IEEE*, and Wei Dai

Abstract—Anomalies usually refer to targets with a spot of pixels (even subpixels) that stand out from their neighboring background clutter pixels in hyperspectral imagery (HSI). Compared to backgrounds, anomalies have two main characteristics. One is the spectral anomaly, i.e., their spectral signatures are different from those associated to their surrounding backgrounds; another is the spatial anomaly, i.e., anomalies occur as few pixels (even subpixels) embedded in the local homogeneous backgrounds. However, most of the existing anomaly detection algorithms for HSI only employed the spectral anomaly. If the two characteristics are exploited in a detection method simultaneously, better performance may be achieved. The third-order (two modes for space and one mode for spectra) tensor representation of HSI has been proved to be an effective tool to describe the spatial and spectral information equivalently; therefore, tensor representation is convenient for exhibiting the two characteristics of anomalies simultaneously. In this paper, a new anomaly detection method based on tensor decomposition is proposed and divided into three steps. Three factor matrices and a core tensor are first estimated from the third-order tensor that is constructed from the HSI data cube by using the Tucker decomposition, and their major and minor principal components (PCs) are more likely to correspond to the spectral signatures of the backgrounds and the anomalies, respectively. In the second step, a reconstruction-error-based method is presented to find the first largest PCs along each mode to eliminate the spectral signatures of the backgrounds as much as possible, and thus, the remaining data may be modeled as the spectral signatures of the anomalies with a Gaussian noise. Finally, a CFAR test is implemented to detect the anomalies from the remaining data. Experiments with simulated, synthetic, and real HSI data sets reveal that the proposed method outperforms those spectral-anomaly-based methods with better detection probability and less false alarm rate.

Index Terms—Anomaly detection, hyperspectral imagery (HSI), tensor representation, Tucker decomposition.

I. INTRODUCTION

COMBINING imaging technology and high spectral resolution spectroscopy in a unique system, the hyperspectral sensor provides a powerful means to discriminate the targets of interest in a scene. In most practical situations, it is difficult to specify the prior spectrum of the interested target in advance.

Manuscript received June 14, 2015; revised November 19, 2015 and February 19, 2016; accepted May 13, 2016. Date of publication June 16, 2016; date of current version August 11, 2016. This work was supported by the Program for New Century Excellent Talents in University of China under Grant NCET-11-0866.

The authors are with the Automatic Target Recognition Laboratory, School of Electronic Science and Engineering, National University of Defense Technology, Changsha 410073, China (e-mail: ppzhangx@sina.cn; wengongjian@sina.com).

Color versions of one or more of the figures in this paper are available online at <http://ieeexplore.ieee.org>.

Digital Object Identifier 10.1109/TGRS.2016.2572400

Therefore, the target detection without any target information, known as anomaly detection, is more preferred and practicable. [1]–[5].

Anomalies usually refer to targets with a spot of pixels (even subpixels) that stand out from the cluttered backgrounds in hyperspectral imagery (HSI), and they have two main characteristics. The first one is the spectral anomaly, i.e., the spectra of anomalies are distinct from those of their surrounding backgrounds. The second one is the spatial anomaly, i.e., anomalies occur as few pixels (even subpixels) embedded in the local homogeneous backgrounds. Various anomaly detection algorithms have been developed by exploiting the two aforementioned characteristics. According to our comprehension, most of the current anomaly detection algorithms place emphasis on the spectral-anomaly characteristic, and they can be classified into two broad categories, i.e., statistical modeling and geometrical modeling techniques.

Statistical modeling techniques commonly assume that the backgrounds follow a specified statistical distribution while anomalies are far away from such distribution. Among the works that belong to this category, the Reed–Xiao detector (RXD) [6] is probably the most popular. In this method, the multivariate Gaussian model is assumed to characterize the background information. After estimating the mean vector and covariance matrix by the samples selected from the whole scene (or a local window), the Mahalanobis distance between each test pixel and the statistical model is calculated and compared with a threshold for the final discrimination. RXD is mathematically tractable and of high computation efficiency. Despite the popularity, there are two main problems with RXD. The first problem is that the unimodal Gaussian model cannot always provide an adequate characterization for the backgrounds, particularly when there are multiple materials. This problem may lead to many false alarms in practice. Various efforts have been made to address such problem. Some approaches are still based on the Gaussian model, but they are designed for making the model more effective. An example is the cluster-based anomaly detection (CBAD) method, which segments the scene into different spectrally homogeneous clusters and then detects anomalies in individual clusters [7]. Another example is the method based on the Gaussian-mixture model, combining a set of unimodal Gaussian distributions to characterize the backgrounds [2], [8]. It provides more accurate descriptions of complex backgrounds by accounting for the presence of multiple materials. Some other methods are based on the non-Gaussian model for a better characterization of the backgrounds in real HSI data, such as the anomaly detection algorithm based on elliptically contoured distribution [9], [10]. In addition, a number

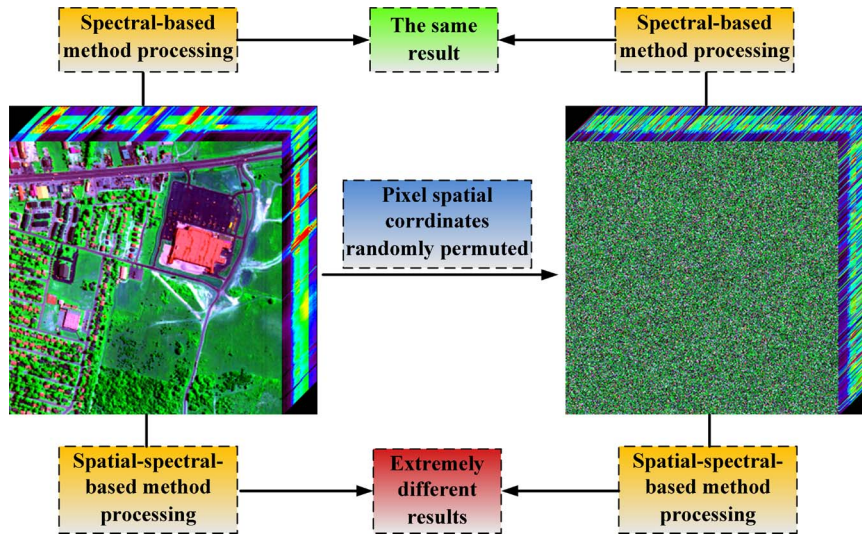


Fig. 1. Example for illustrating the different results of spectral-based and spectral-spatial-based anomaly detection methods.

of authors have observed that the data can be more Gaussian in some directions than in others, so a hybrid Gaussian/non-Gaussian algorithm was proposed in [11]. This method can explicitly produce a probability density that is a product of the multivariate Gaussian density in the Gaussian directions and a more tailored distribution in the non-Gaussian directions. The second problem is that the background samples often contain also anomalous pixels and noise, which causes that the parameters of the statistical model cannot be estimated accurately, resulting in a poor detection performance. To mitigate the contamination of anomalous signatures when estimating the background model, a lot of anomaly detection algorithms have been proposed, such as the blocked adaptive computationally efficient outlier nominator method [12], minimum covariance determinant method [13], random-selection-based anomaly detector [14], robust nonlinear anomaly detection (RNAD) [15], weighted RXD [16], and discriminative metric learning-based anomaly detection [17].

Geometrical modeling techniques are based on the key assumption that background pixels can be approximately represented by a group of the major spectra/bases, while anomalies cannot. Those spectra/bases are collected/extracted from the whole image (or a local window). This type of method avoids assuming any specific statistical model for the backgrounds. As for this category, the subspace-based anomaly detection method is the most typical [18]. This method assumes that the background is well modeled as lying in a low-dimensional subspace that is constructed by a set of bases, which are commonly derived from background endmembers (corresponding to major and pure materials in the image) extracted from the data or eigenvectors acquired by a linear transformation (e.g., SVD). Then, every pixel is projected to the background orthogonal subspace, and the residual is calculated for discriminating whether the current pixel is an anomaly. The larger the residual is, the more anomalous the pixel may be. Some other methods use the original spectra of the whole scene and a local window to represent each pixel. The pixel with a large reconstruction residual is more probable to be an anomaly.

The sparse-representation-based detector [19], [20] and collaborative-representation-based detector (CRD) [21] belong to this category.

However, both of the two aforementioned techniques only deal with vector features as inputs, known as the vector-based anomaly detection method. In other words, they just process each pixel as a spectral vector independently, without considering the spatial relationship between different pixels. In those techniques, only the spectral-anomaly characteristic of an anomaly is exploited. Some researchers suggest that considering the neighboring pixels can employ the spatial information, such as the local RX [22], dual-window-based eigen separation transform (DWEST) [23], and multiple-window anomaly detection [24]. Nevertheless, these methods just analyze the spectral difference in a relatively smaller region; neither the spatial constraints between each pixel in the current local window nor the spatial relationship between different local windows is taken into consideration. As a result, the spectral information is much superior to the spatial information in those methods. The spatial anomaly is equivalently important as the spectral anomaly, which means that an anomaly is not only spectrally distinct from the spectral-homogeneous backgrounds but also spatially isolated in an agglomeration of backgrounds. It is clear that, if the two characteristics are exploited in an anomaly detection method simultaneously, then better performance may be achieved. To the best of our knowledge, there is still no method that describes spectral anomaly equivalently with regard to the spatial anomaly in an anomaly detection algorithm.

An example of the different results of spectral-based anomaly detector and spectral-spatial-based anomaly detector is given in Fig. 1, in which an HSI data cube collected over an urban area (high spatial correlation) is modified by randomly permuting the spatial coordinates (i, j) of the pixel vectors, thus removing the spatial correlation. In both scenes, the application of a spectral-based anomaly detector would yield the same analysis results, while it is clear that, if the spectral-anomaly and spatial-anomaly characteristics are jointly exploited (known as the spectral-spatial-based method), the detection results should be

extremely different. Hence, the spatial information present in the original data may not be ignored in the anomaly detection process.

In this paper, we propose a method for spectral–spatial anomaly detection in a novel point of view, which is based on tensor decomposition. As indicated in some previous works within the HSI data processing area, tensor representation has been proved useful for analyzing the three-factor structure of HSI in many fields, such as feature extraction [25], data compression [26], denoising [27], [28], classification [29], [30], and material identification [31]. HSI data can be intrinsically treated as a three-order tensor (two modes for space and one mode for spectra); by this way, both the spatial and spectral information can be described equivalently, and it is convenient for exhibiting the spectral anomaly and spatial anomaly simultaneously. The proposed algorithm contains three main steps. First, we employ a three-order tensor to represent the observed HSI data cube and introduce the Tucker decomposition technology to decompose such tensor into a core tensor and three factor matrices. Thus, the major and minor principal components (PCs) of the three factor matrices are likely to correspond to the background and the anomaly information, respectively. Second, a reconstruction-error-based method is present to find the first largest PCs along each mode to eliminate the background information as much as possible, and thus, the remaining data may be modeled as the anomaly with a Gaussian noise. Finally, a CFAR test is implemented to detect the anomalies from the remaining data.

The remainder of this paper is arranged as follows. In Section II, we give a brief description of the relevant tensor algebra and then present the proposed anomaly detection algorithm based on the Tucker decomposition in detail. After that, the experimental results are reported in Section III, followed by the conclusion.

II. PROPOSED ANOMALY DETECTION ALGORITHM

In this section, we first give a brief review of the relevant concepts for tensor algebra that will be used in the proposed algorithm.

For an N -order tensor, $\mathcal{X} \in R^{I_1 \times I_2 \times \dots \times I_N}$, where $I_n (1 \leq n \leq N)$ shows the size of this tensor in each mode and an arbitrary element of \mathcal{X} is a scalar denoted by $x_{i_1 i_2 \dots i_N}$, in which each i_n addresses the n -mode of \mathcal{X} and $1 \leq i_n \leq I_n$. The n -mode unfolding of \mathcal{X} is denoted by keeping the index i_n fixed and varying the other indices, which is denoted as $X_{(n)} \in R^{I_n \times \prod_{i=1, i \neq n}^N I_i}$. The n -mode rank of \mathcal{X} , denoted as $\text{rank}_n(\mathcal{X})$, is the column rank of $X_{(n)}$. If we let $R_n = \text{rank}_n(\mathcal{X})$ for $n = 1, 2, 3, \dots, N$, then we can say that \mathcal{X} is a rank- $(R_1, R_2, R_3, \dots, R_N)$ tensor. The n -mode product of a tensor \mathcal{X} by a matrix $A \in R^{J \times I_n}$ is a tensor with entries $(\mathcal{X} \times_n A) \in R^{I_1 \times \dots \times I_{n-1} \times J \times I_{n+1} \times \dots \times I_N}$. For more details, refer to [32] and [33].

By employing the tensor representation and decomposition technologies, the proposed algorithm (abbreviated as TenB in the rest of this paper) is divided into three main steps, as shown in Fig. 2.

A. Three-Order Tensor Representation and Decomposition for HSI Data Cube

An HSI data cube is represented by a three-order tensor $\mathcal{X} \in R^{I_1 \times I_2 \times I_3}$, where I_1 , I_2 , and I_3 indicate the image height, image width, and spectral channels of HSI, respectively. $x_{i_1 i_2 i_3}$ ($1 \leq i_n \leq I_n, n = 1, 2, 3$) is related to the point that is locating at pixel- (i_1, i_2) and spectral band- i_3 . If the HSI data cube is considered independent along each mode, we can get the fiber analogs of such data (as shown in Fig. 3). It is noteworthy that, for a routine spectral-based anomaly detection technique, the HSI data are processed as the spectral vector form. In other words, each spectrum is treated independently, without considering the spatial constraints.

Then, the Tucker decomposition [33], [34] is applied onto the tensor \mathcal{X} ; as a result, three factor matrices along the three modes and a core tensor are obtained, shown in (1) as follows:

$$\mathcal{X} \approx G \times_1 A \times_2 B \times_3 C \quad (1)$$

in which $A \in R^{I_1 \times J_1}$, $B \in R^{I_2 \times J_2}$, and $C \in R^{I_3 \times J_3}$ are the factor matrices. The tensor $G \in R^{J_1 \times J_2 \times J_3}$ is called the core tensor, and its elements $g_{i_1 i_2 i_3}$ represent the level of interaction between the different components. Elementwise, the Tucker decomposition in (1) is

$$x_{i_1 i_2 i_3} = \sum_{j_1=1}^{J_1} \sum_{j_2=1}^{J_2} \sum_{j_3=1}^{J_3} g_{j_1 j_2 j_3} a_{i_1 j_1} b_{i_2 j_2} c_{i_3 j_3}. \quad (2)$$

Here, J_1 , J_2 , and J_3 denote the number of components (i.e., columns) in the factor matrices A, B, and C, respectively. Fig. 4(a) illustrates the Tucker decomposition on a three-order tensor, and Fig. 4(b) gives an example for the elementwise representation of such decomposition.

The optimization problem for the Tucker decomposition that we wish to solve is

$$\begin{cases} f = \min_{G, A, B, C} \|\mathcal{X} - G \times_1 A \times_2 B \times_3 C\|_F^2 \\ \text{subject to } G \in R^{J_1 \times J_2 \times J_3}, \\ A \in R^{I_1 \times J_1}, B \in R^{I_2 \times J_2}, C \in R^{I_3 \times J_3}, \\ A^T A = I, B^T B = I, C^T C = I. \end{cases} \quad (3)$$

Since A, B, and C have orthonormal columns, from (3), we can obtain $G \approx \mathcal{X} \times_1 A^T \times_2 B^T \times_3 C^T$. As stated in [34], the minimization in (3) is equivalent to the maximization of the function

$$\begin{cases} g = \max_{A, B, C} \|X \times_1 A^T \times_2 B^T \times_3 C^T\|_F^2 \\ \text{subject to } A \in R^{I_1 \times J_1}, B \in R^{I_2 \times J_2}, C \in R^{I_3 \times J_3}, \\ A^T A = I, B^T B = I, C^T C = I. \end{cases} \quad (4)$$

To solve the optimal problem in (4), the alternating least squares algorithm [35], [36] is feasible and usually employed, which was developed by Kroonenberg and De Leeuw [37] in 1980 for a three-order tensor. The basic idea of this solution comes from the fact that any one of the factor matrices could be simply acquired by an eigenvalue decomposition problem when the remaining two matrices are fixed. Trivially, $J_n < I_n$ ($n = 1, 2, 3$), meaning that the Tucker decomposition offers a straightforward approach of compression for preserving the

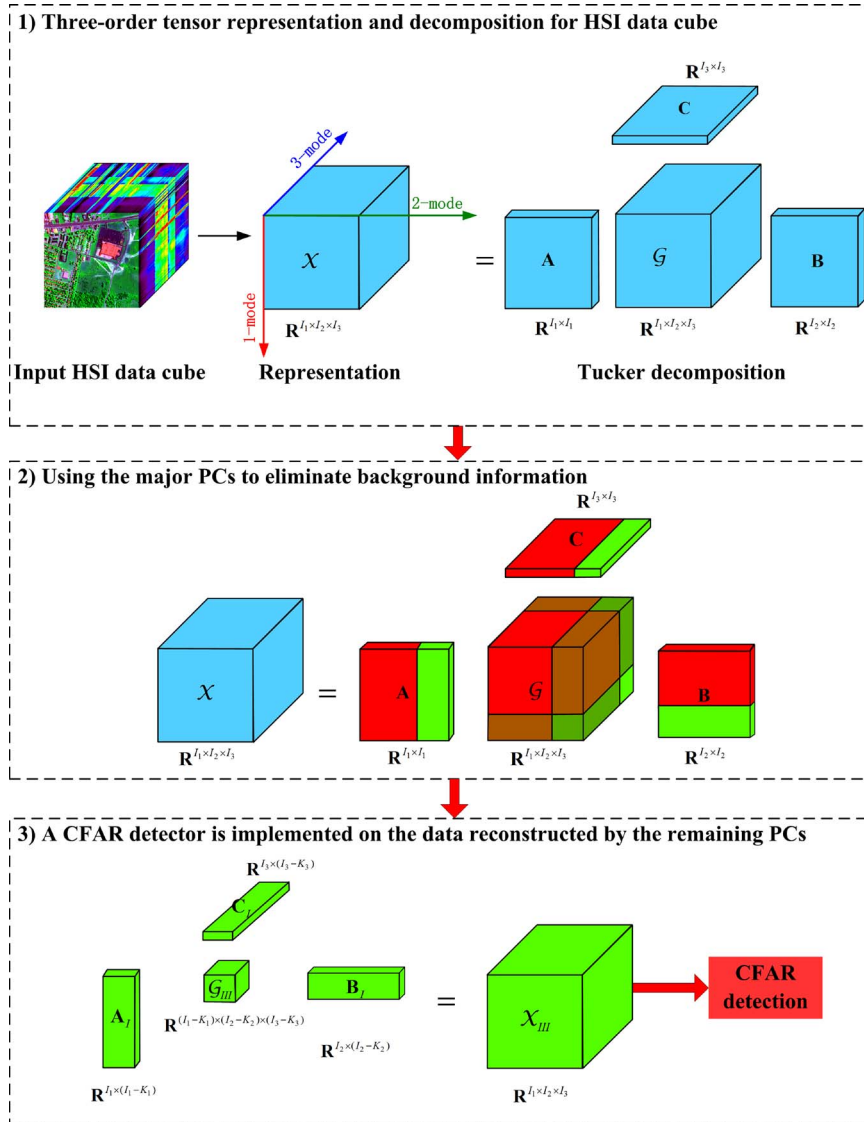


Fig. 2. Flowchart of the proposed approach.

most significant information, with the insignificant information being truncated. However, in this paper, our aim is to extract the anomaly signals from the data, and the anomaly signals may quite possibly exist in the insignificant part. Therefore, we permit $J_n = I_n$ ($n = 1, 2, 3$), for the purpose of maintaining the complete information which is composed by all the eigenvalues and eigenvectors. Therewith, all the three factor matrices A , B , and C are square, and the size of the core tensor is the same with the input tensor.

In fact, the Tucker decomposition is a form of higher order PCA; as a result, the column eigenvectors of each factor matrix are ordered by decreasing magnitude of the respective eigenvalues. If each eigenvector is interpreted as a piece of information, the larger the eigenvalue is, the more significant the information that it represents. Generally, in an HSI, backgrounds turn up with high probabilities as the major information, while anomalies occur with low probabilities as minor information. Under this circumstance, the first largest eigenvectors of each factor matrix represent the components that address the background information along each mode, while the anomalies are probably

to lie in the remaining eigenvectors. Here, we give an example for illustrating the spatial-anomaly characteristic captured by the tensor representation technique. In Fig. 5(a), there is an HSI data cube with a spatial size of 11×11 . The main background pixels are colored red. Another 3×3 sized background colored blue is in the center, and an anomaly pixel locating at pixel-(10, 10) is colored yellow. According to the one-mode fiber analog of the tensor (see Fig. 3), the more image height vectors an object contains, the more column information it owns. Consequently, the corresponding eigenvector of such object is likely to be more former in A , while on the opposite side, the eigenvector of the object that contains less image height vectors may be ranked latter. Analogically, it is the same with the image width mode. An anomalous target may be neither wider nor longer than the backgrounds. Therefore, the eigenvectors of anomalous targets are ranked latter in the factor matrices. This is just the embodiment of the spatial-anomaly characteristic. Taking the first band of the HSI for example, it contains three types of vectors: 1) with 11 red pixels; 2) with 8 red pixels and 3 blue pixels; and 3) with 10 red pixels and 1 green pixel. Their

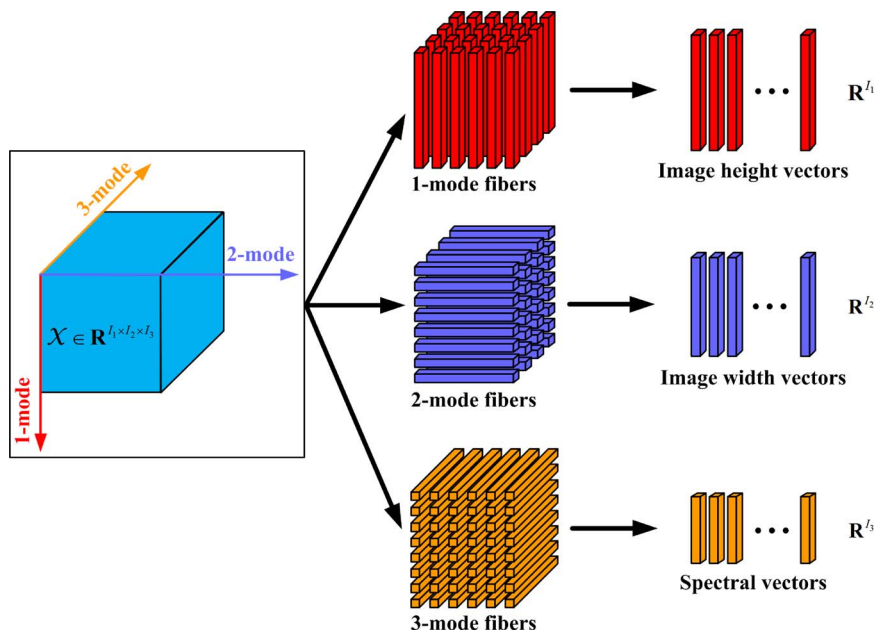


Fig. 3. Three fiber analogs of an HSI data cube.

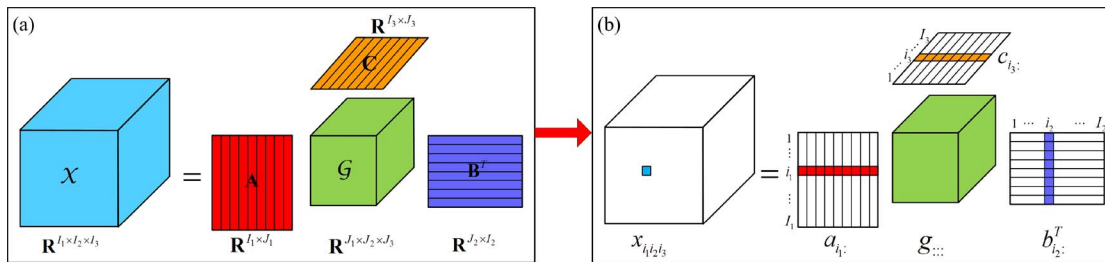


Fig. 4. Visual illustration of the Tucker decomposition. (a) Tucker decomposition on a three-order tensor. (b) Example for the elementwise representation of such decomposition.

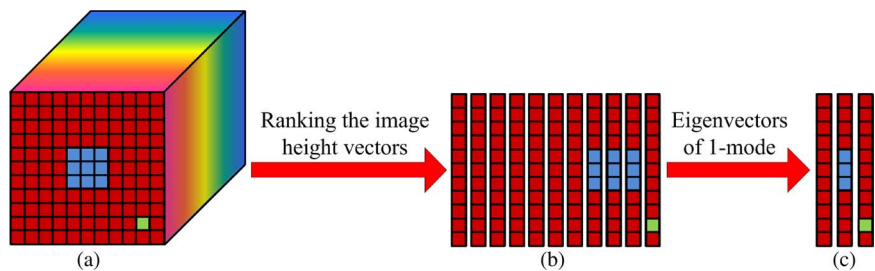


Fig. 5. Example for illustrating the spatial-anomaly characteristic captured by the tensor representation technique. (a) HSI data cube with two backgrounds and an anomaly. (b) Result of the image height vectors (the first band) ranked in line with the number of vectors. (c) Eigenvectors for representing those vectors in (b).

numbers are 7, 3, and 1, respectively. The result of the image height vectors ranked in line with their numbers is shown in Fig. 5(b). In fact, the same vectors may be represented by one eigenvector. Therefore, three eigenvectors [shown in Fig. 5(c)] are needed to represent the data in Fig. 5(b). It can be seen that the eigenvectors corresponding to the background are ranked more former than the anomalies.

B. Using the Major PCs to Eliminate Background Information

To detect anomalies effectively, one of the key challenges is to eliminate the background that presents as interfering

signatures. Traditional spectral-based methods represent the background information by a set of spectral vectors $x_i \in R^{I_3} (1 \leq i \leq I_1 I_2)$, in which I_3 gives the spectral channels and $I_1 I_2$ is the total number of pixels in HSI. Consequently, this branch of approaches only eliminates the backgrounds in the spectral domain. Among those kinds of anomaly detectors, SSRX [38] is the most popular one, which is a modification to the RXD. In SSRX, several high-variance PCs are deleted before applying the RXD, as these PCs are assumed to capture nonnormal background clutter variance. In this case, determining the number of the major PCs (e.g., K) is crucial. K is chosen to capture background information as much as possible

while hopefully not containing anomaly content. Unfortunately, there is no reliable method to select an optimal value for the parameter automatically so far. The energy-cumulative method is used most commonly. It computes the sum of the eigenvalues from the first to the last one, until the cumulative energy achieves a specified ratio to the total energy. In this method, the ratio is difficult to determine for different HSI data sets, and it holds no physical meaning. Under certain conditions, SSRX can provide better background suppression relative to the RXD if the anomaly content falls outside the leading PCs.

In contrast, the proposed TenB algorithm eliminates background information along the three modes simultaneously. That is to say, background information is assumed to be represented by both the major PCs in the spectral and spatial domains. In a real-world situation, the background pixels belonging to the same kind may be likely to huddle together. As a result, background information not only dominates in the spectral domain but also in the spatial domain. Therefore, it can make sure that background information could be eliminated more exhaustively by this way.

Similar to SSRX, the PC numbers also need to be determined in TenB. In this paper, we employ a reconstruction-error-based method to deal with this problem, described as follows. \mathcal{X}_{Bg} is defined as the estimated background of \mathcal{X} , and the relative reconstruction error between \mathcal{X}_{Bg} and \mathcal{X} is denoted as $\varepsilon = \|\mathcal{X} - \mathcal{X}_{Bg}\|/\|\mathcal{X}\|$. As K goes up from 0 to the max PC number, ε descends from 1 to 0. The smaller ε is, the more information of \mathcal{X} is preserved in \mathcal{X}_{Bg} . It is assumed that each major PC may represent one or more kinds of background. Therefore, when ε leaps down, it indicates that a new major material (much possibly a kind of background) appears in \mathcal{X}_{Bg} ; in the other side, when ε decreases slowly, it indicates that some minor material is added to \mathcal{X}_{Bg} . Under these assumptions, the first point of slow change is used to determine K . This method owns better applicability than the traditional energy-cumulative method, and it can be interpreted in a physical way.

There are three PC numbers (e.g., K_1 , K_2 , and K_3 along each mode, respectively) needed to be determined in TenB. Here, we give the process of determining K_1 for example. First, the tensor \mathcal{X} is unfolded along the image height mode, resulting in a matrix denoted as $X_{(1)} \in \mathbf{R}^{I_1 \times (I_2 I_3)}$. Second, SVD is applied onto $X_{(1)}$, and the corresponding eigenvectors (denoted as $v_{(1)} = [v_{(1)}^1, v_{(1)}^2, \dots, v_{(1)}^{I_1}]$, $v_{(1)}^i \in \mathbf{R}^{I_1}$) are obtained. Third, the first eigenvector to the last eigenvector is selected one by one to reconstruct the background of $X_{(1)}$, denoted as $X_{(1)}^{Bg}$. The relative reconstruction error ε_1 between $X_{(1)}$ and $X_{(1)}^{Bg}$ is computed, and the first point of ε_1 that changes slowly is determined for K_1 . It is assumed that the first K_1 largest PCs of $X_{(1)}$ delegate the major information along the image height mode. Analogically, K_2 and K_3 can be determined in the same manner, and they delegate the major information along the image width mode and spectral mode, respectively.

As K_i ($i = 1, 2, 3$) have been determined, all the three factor matrices can be divided into two parts. Such two sub A matrices, referred to as $A_S \in \mathbf{R}^{I_1 \times K_1}$ and $A_I \in \mathbf{R}^{I_1 \times (I_1 - K_1)}$, indicate the significant and insignificant parts of factor matrix A; by analogy, $B_S \in \mathbf{R}^{I_2 \times K_2}$ and $B_I \in \mathbf{R}^{I_2 \times (I_2 - K_2)}$ are the

two parts of B, and $C_S \in \mathbf{R}^{I_3 \times K_3}$ and $C_I \in \mathbf{R}^{I_3 \times (I_3 - K_3)}$ are the two parts of C. Correspondingly, the core tensor \mathcal{G} is divided into eight parts: $\mathcal{G}_{SSS} \in \mathbf{R}^{K_1 \times K_2 \times K_3}$, $\mathcal{G}_{ISS} \in \mathbf{R}^{(I_1 - K_1) \times K_2 \times K_3}$, $\mathcal{G}_{SIS} \in \mathbf{R}^{K_1 \times (I_2 - K_2) \times K_3}$, $\mathcal{G}_{IIS} \in \mathbf{R}^{(I_1 - K_1) \times (I_2 - K_2) \times K_3}$, $\mathcal{G}_{SSI} \in \mathbf{R}^{K_1 \times K_2 \times (I_3 - K_3)}$, $\mathcal{G}_{ISI} \in \mathbf{R}^{(I_1 - K_1) \times K_2 \times (I_3 - K_3)}$, $\mathcal{G}_{SII} \in \mathbf{R}^{K_1 \times (I_2 - K_2) \times (I_3 - K_3)}$, and $\mathcal{G}_{III} \in \mathbf{R}^{(I_1 - K_1) \times (I_2 - K_2) \times (I_3 - K_3)}$. In Fig. 2-2), the red color part of each matrix indicates the significant PCs, and the green color indicates the insignificant PCs, respectively. The same color indications are present in the core tensor.

Three subfactor matrices along each mode and one corresponding subcore tensor can reconstruct a tensor with the same size as tensor \mathcal{X} , so there are eight subtensors that can be reconstructed, which are listed as $\mathcal{X}_{SSS}, \mathcal{X}_{ISS}, \mathcal{X}_{SIS}, \mathcal{X}_{IIS}, \mathcal{X}_{SSI}, \mathcal{X}_{ISI}, \mathcal{X}_{SII}, \mathcal{X}_{III}$, correspondingly. For example, the first subtensor is reconstructed as

$$\begin{cases} \mathcal{X}_{SSS} = \mathcal{G}_{SSS} \times_1 A_S \times_2 B_S \times_3 C_S \\ \text{where } \mathcal{G}_{SSS} = \mathcal{G}_{1:K_1, 1:K_2, 1:K_3} \\ A_S = A_{:, 1:K_1}, B_S = B_{:, 1:K_2}, C_S = C_{:, 1:K_3}. \end{cases} \quad (5)$$

It is worth noting that the size of every reconstructed tensor is equivalent to that of the input HSI data. As a linear transformation, the Tucker decomposition satisfies the additional rule. Hence, the sum of the eight subtensors is equal to the original tensor. Here, we have

$$\begin{aligned} \mathcal{X} = & \mathcal{X}_{SSS} + \mathcal{X}_{ISS} + \mathcal{X}_{SIS} + \mathcal{X}_{IIS} + \mathcal{X}_{SSI} \\ & + \mathcal{X}_{ISI} + \mathcal{X}_{SII} + \mathcal{X}_{III}. \end{aligned} \quad (6)$$

We assume that the background information is composed of the significant part along every mode and the anomalies are contained in the remaining part. Therefore, the background information is represented by

$$\mathcal{X}_{Bg} = \mathcal{X}_{SSS} + \mathcal{X}_{ISS} + \mathcal{X}_{SIS} + \mathcal{X}_{IIS} + \mathcal{X}_{SSI} + \mathcal{X}_{ISI} + \mathcal{X}_{SII}. \quad (7)$$

Notably, the SSRX is a special version of TenB, when the TenB method just processes the data along the spectral mode, known as TenB3. In other words, when the background information is estimated only by the major PCs of $X_{(3)}$, SSRX is equivalent to TenB3. This conclusion will be verified in the experimental reports.

C. CFAR Detector Is Implemented on the Data Reconstructed by the Remaining PCs

When the number of major PCs is set properly, the background information can be well eliminated; then, the anomaly may possibly lie in the remaining data \mathcal{X}_{An} . Such \mathcal{X}_{An} is assumed to be modeled as the anomaly signatures with a Gaussian noise. Under this condition, a CFAR detection algorithm is expected to detect the anomalies because the CFAR detection algorithm considered in [39] is suitable for detecting a target pattern in one main image scene and a number of other noise-only reference image scenes that contain negligible signal energy.

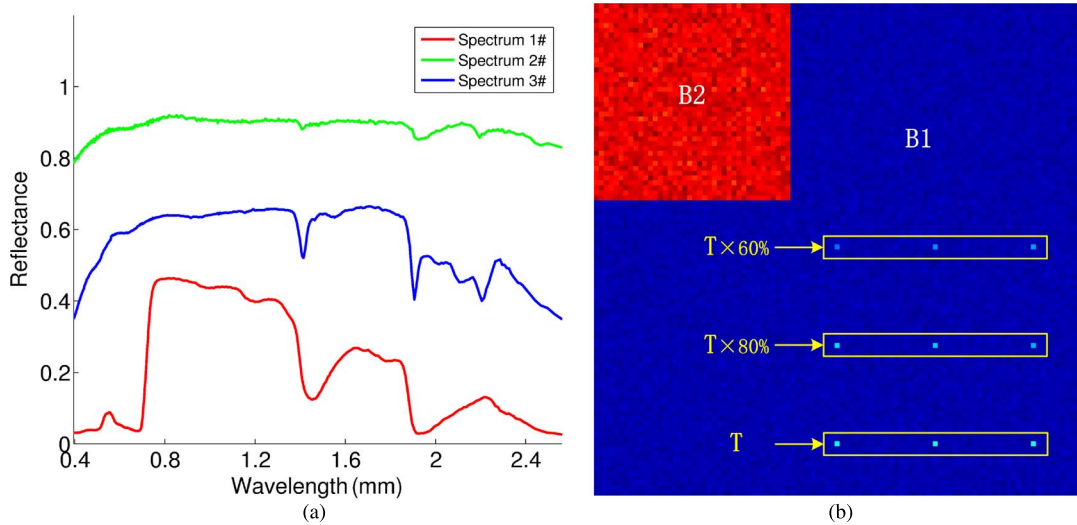


Fig. 6. Simulated HSI data. (a) Three selected spectra of three different materials. (b) First band of the data.

Let each spectrum in \mathcal{X}_{An} be denoted by $\mathbf{x} = [x_1, x_2, \dots, x_L]^T \in R^L$. Define \mathbf{X}_b to be an $L \times N$ matrix, where N denotes the pixel number of the whole image and each pixel is represented as a column in the sample matrix \mathbf{X}_b . The two competing hypotheses that the CFAR must distinguish are given by

$$\begin{aligned} \mathbf{H}_0 : \mathbf{x} &= \mathbf{n} \text{ (Anomaly absent)} \\ \mathbf{H}_1 : \mathbf{x} &= a\mathbf{s} + \mathbf{n} \text{ (Anomaly present)} \end{aligned} \quad (8)$$

where \mathbf{n} is a vector that represents the noise and \mathbf{s} is the anomaly spectral signature given by $\mathbf{s} = [s_1, s_2, \dots, s_L]^T$. The model assumes that the data arise from two normal probability density functions with the same covariance matrix but different means. Under \mathbf{H}_0 , the noise is modeled as $N(\boldsymbol{\mu}_n, \mathbf{C}_n)$, and under \mathbf{H}_1 , the data are modeled as $N(\boldsymbol{\mu}_n + \mathbf{s}, \mathbf{C}_n)$. $\boldsymbol{\mu}_n$ and \mathbf{C}_n are the noise mean and covariance. Assuming a single pixel \mathbf{r} as the observation test spectrum, the output of the CFAR is given by

$$D_{\text{CFAR}}(\mathbf{r}) = (\mathbf{r} - \boldsymbol{\mu}_n)^T \mathbf{C}_n^{-1} (\mathbf{r} - \boldsymbol{\mu}_n). \quad (9)$$

III. EXPERIMENTAL RESULTS

In order to illustrate the superiority of TenB in background estimation and anomaly detection, a detailed analysis for a simulated HSI data set was given at first. Then, the experimental analysis was done on both synthetic and real HSI data sets.

A. Data Set Description

Simulated Data: We use three reflectance spectra [coverage from 400 to 2500 nm with a total of 420 bands, shown in [Fig. 6(a)] representing aspen_leaf, albite, and smectite as downloaded from the USGS spectroscopy library [40] to generated an HSI data set. The three materials are identified as ‘‘Aspen_Leaf-A DW92-2’’ (Spectrum 1[#]), ‘‘Albite HS66’’ (Spectrum 2[#]), and ‘‘Ammonio-Smectite GDS86’’ (Spectrum 3[#]).

The size of the simulated HSI is 100×100 . First, Spectrum 1[#] is used to fill the whole data, as one kind of background (denoted as B_1). Then, a 40×40 block in the upper left corner is replaced by Spectrum 2[#], as another kind of background (denoted as B_2). In addition, nine anomalous targets (denoted as T) are implanted into the data. We generate the anomalous targets using a synthetic spectral signature \mathbf{z} with a specified abundance fraction f from a desired target \mathbf{t} , contaminated by a background signature \mathbf{b} [41], [42]. For the simulations, we use a simple linear mixture model as follows:

$$\mathbf{z} = f \cdot \mathbf{t} + (1 - f) \cdot \mathbf{b}. \quad (10)$$

Here, we consider the Spectrum 3[#] as \mathbf{t} and Spectrum 1[#] as \mathbf{b} . According to (10), the anomalous targets are implanted with the abundance fractions $f = 0.6, 0.8$, and 1 for each row, respectively. Furthermore, 30-dB Gaussian white noise is added into the data set. Fig. 6(b) shows the first band of the simulated HSI data.

Synthetic Data: The synthetic data were generated using a Hyperion data set covering an agricultural area. It was downloaded from the EO-1 satellite image website. The original data set contains 242 bands covering the visible, near-infrared, and short-wave infrared bands (400–2500 nm) with a spectral resolution of 10 nm. After the removal of the low-SNR bands and the uncalibrated bands, 193 bands are used. The selected portion (illustrated in Fig. 7) has pixels of 120×180 in size.

In this paper, we have decided to use a target implantation method to simulate a set of anomalous targets in the considered Hyperion data set. The advantage of using a target implantation method is that we can evaluate the performance of the detectors in a totally controlled environment [43]. The image portion where the targets have been implanted is denoted as ROI-1 [see Fig. 7(a)], which is an open vegetation region with dimensions $120 \times 180 \times 193$ and contains a few anomalous pixels. Four types of vegetation can be considered as the main background in this region. Their spectra are shown in Fig. 7(b) with high correlation to each other (denoted as B_1, B_2, B_3 , and B_4).

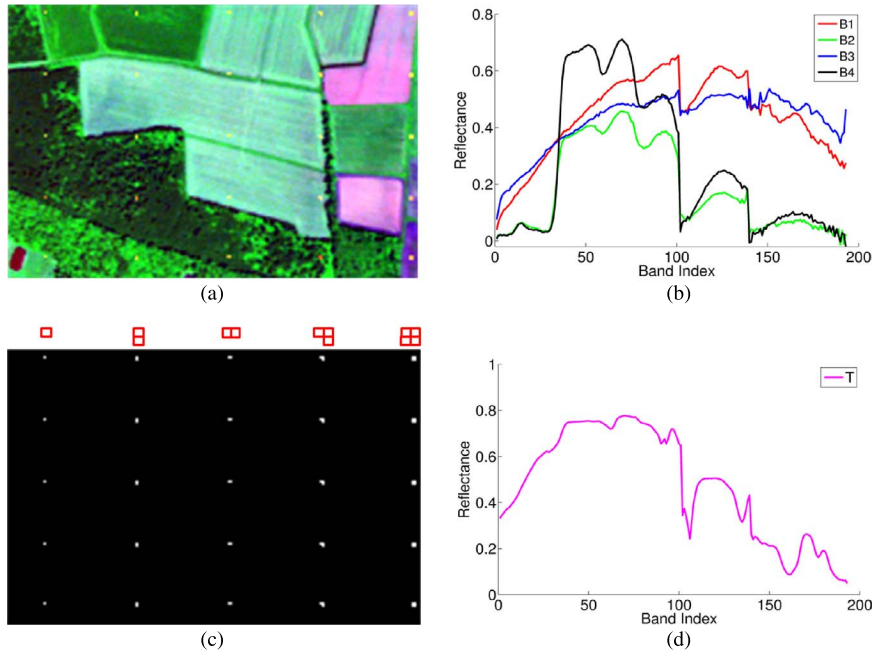


Fig. 7. Hyperion data set (ROI-1) for experiment. (a) False color image of the scene with implanted targets. (b) Spectra of the four main backgrounds. (c) Locations of the implanted targets. (d) Target spectrum.

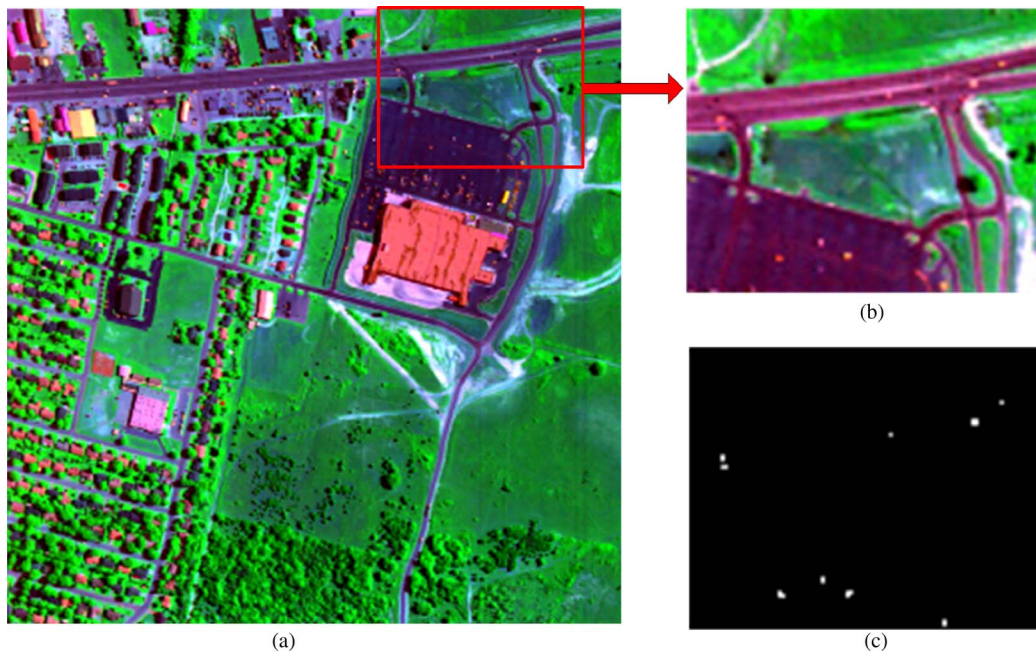


Fig. 8. HYDICE data set for experiment. (a) False color of the original data set. (b) False color of ROI-2 scene. (c) True distribution of all the anomalous targets in ROI-2.

Some background-background mixed pixels are present on the background boundary. The characteristic of the target is selected from the original image that is the most different from the main background endmembers. Fig. 7(d) shows the target spectrum (denoted as T). 5×5 targets have been implanted into ROI-1 using (10), where the abundance fractions $f = 0.8, 0.65, 0.5, 0.35,$ and 0.2 for each row, respectively. The sizes of targets are different in each column, with 1×1 pixel, 2×1 pixels, 1×2 pixels, 3 pixels, and 2×2 pixels in each column, respectively. Fig. 7(c) shows the locations of the implanted targets in ROI-1,

and the details of the targets' shape are listed on the top. The percentage of target pixels in the entire image is approximately 0.3%.

Real Data 1: A Hyperspectral Digital Imagery Collection Experiment (HYDICE) hyperspectral data set is obtained from an aircraft platform. This data set covers an urban area and has a spectral resolution of 10 nm and a spatial resolution of 1 m. The image scene contains a vegetation area, a construction area, and several roads, where there are some vehicles. The HYDICE imaging sensor generates 210 bands covering the

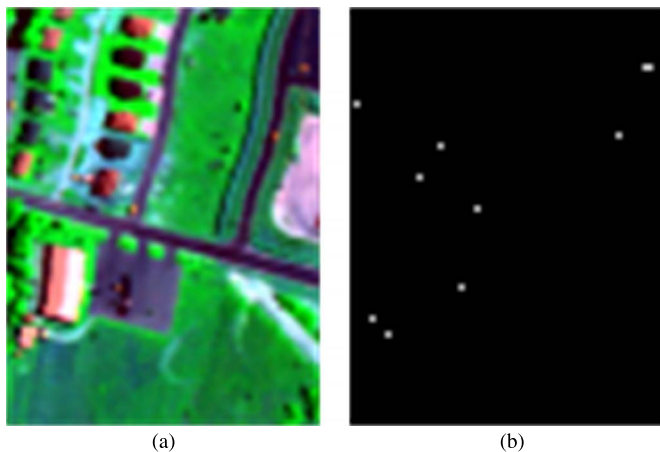


Fig. 9. ROI-3 for experiment. (a) False color of the scene. (b) True distribution of all the anomalous targets in ROI-3.

whole spectral range of 400–2500 nm, but only 162 spectral bands are used after discarding the water absorption and low-SNR bands. The false color image of the whole data set has a size of 307×307 , as shown in Fig. 8(a). However, the only definite ground truth is that, in the upper right of the scene, the anomalous targets are the vehicles embedded in the different backgrounds. Therefore, we only use the subimage covering this area in our experiments. A scene of 79×100 pixels called ROI-2 [see Fig. 8(b)] and the anomalous targets' positions are shown in Fig. 8(c). There are nine vehicles with 20 pixels in total, which are regarded as the anomalous targets in the scene.

Real Data 2: This data set is also cut from the HYDICE data set. The scene consists of 80×60 pixels [as shown in Fig. 9(a)] with 162 bands, denoted as ROI-3. There are nine vehicles with 10 pixels in total, which are regarded as the anomalous targets in the scene [see Fig. 9(b)]. Compared to ROI-2, ROI-3 is more complex with grass, tree, road, park, and buildings (with different materials and shapes). Furthermore, some of the anomalous targets are difficult to be detected, including the targets in the background-background mixing area, near the buildings, and even in the shadow of the buildings.

B. Experimental Results and Analysis

The RXD [6] and SSRX [38] detectors are known to be the standard anomaly detectors that form the basis for comparing the performance of a new anomaly detector. In our experiments, the SSRX algorithm is used for comparing with the TenB algorithm in background elimination. Furthermore, we choose several other conventional anomaly detection methods for evaluation and comparison in the performance of anomaly detection, including CBAD [7], RNAD [15], CRD [21], and DWEST [23].

Since the images produced by the detection algorithms are generally grayscale, the target detection and discrimination are usually carried out by visual inspection. In order to avoid such human interpretation and illustrate a more intuitionistic comparison, an adaptive thresholding method [44] is designed to automatically select an appropriate threshold to segment targets from the image background. This method is adaptive and

only depends on the grayscale image resulting from anomaly detection, but not on the original image. The threshold is computed by

$$\Delta = u + (M - u) \cdot \sqrt{\frac{u}{M}} \quad (11)$$

where u is the mean value and M is the max value of the grayscale image G derived from the detection result. Generally, G is with the same spatial size of the processed data. Each pixel's value (having been normalized to 0-255) in G indicates the detection energy of the corresponding pixel in the input data. Every anomaly detector can gain a G . Then, we compute u and M from the individual G and construct the corresponding threshold Δ .

Detection performance is commonly measured in terms of receiver operating characteristic (ROC) curves [45]. By taking a threshold, the detection result can be transformed to a binary image, where value 1 represents that targets are present in the pixel and value 0 represents that targets are absent. Based on the ground truth, by taking all possible thresholds, the ROC curve can plot the varying relationship between the detection probability P_d and false alarm rate P_f , which are defined as

$$P_d = \frac{N_{\text{detection}}}{N_{\text{total}}} \quad P_f = \frac{N_{\text{false}}}{N_{\text{image}}} \quad (12)$$

where $N_{\text{detection}}$ represents the number of anomalous target pixels detected under a certain threshold and N_{total} represents the total number of anomalous target pixels in the image; N_{false} represents the number of background pixels having been detected, and N_{image} represents the total pixel number of the image. A superior detector would lie nearer the top left or a larger area under the curve (AUC). Moreover, the AUC is computed to evaluate the detection performance for further validation.

1) Experiment 1—Simulated HSI Data:

a) *Background estimation:* As mentioned earlier in Section II-B, the relative reconstruction error ε is considered as an important criterion for evaluating the performance of background estimation. Fig. 10 shows the different ε with the number of the major PCs increasing, where TenB1, TenB2, and TenB3 denote the reconstruction background data \mathcal{X}_{Bg} acquired along the three different modes, respectively. For example, the \mathcal{X}_{Bg}^1 is reconstructed from the first PC to the last PC along the image height mode while keeping the other two modes with their full PCs, defined as

$$(\mathcal{X}_{Bg}^1)_i = \mathcal{G}_i^1 \times {}_1A_i \times {}_2B \times {}_3C \quad (13)$$

where $\mathcal{G}_i^1 \in R^{i \times I_2 \times I_3}$, $A_i \in R^{I_1 \times i}$, $B \in R^{I_2 \times I_2}$, $C \in R^{I_3 \times I_3}$, $1 \leq i \leq I_1$.

From Fig. 10, we can see that, as the number of the PCs increases, ε decreases. This phenomenon illuminates that the information is preserved more completely in \mathcal{X}_{Bg} when the PC number is larger. Fig. 10(a) shows that, when the PC number rises from one to two, ε slumps, and when the PC number keeps going up from three, ε decreases slowly. This phenomenon demonstrates that the major information along

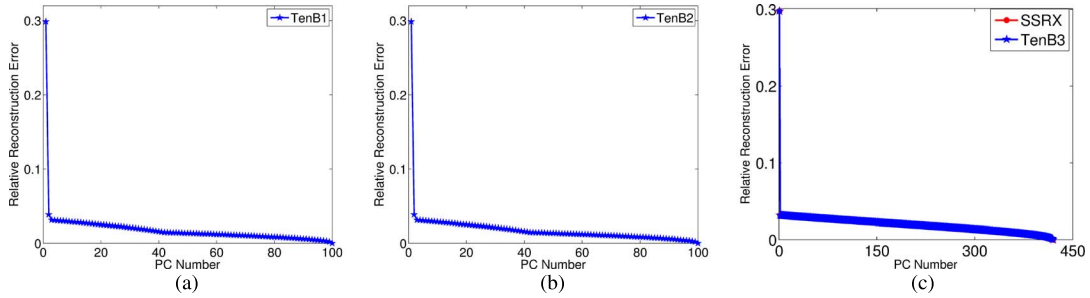


Fig. 10. Relative reconstruction error curves of simulated HSI data. (a) TenB method along the first mode. (b) TenB method along the second mode. (c) TenB method along the third mode and SSRX method.

the image height mode is contained in the first two PCs. The same conclusion could be drawn from Fig. 10(b). Fig. 10(c) has verified the conclusion that SSRX is equivalent to TenB3 and the PC number can be determined as one.

Aside from the relative reconstruction error, the reconstructed spectral curves are also considered to evaluate the background estimation. If the background is estimated accurately, the spectral curves of different materials may be well reconstructed. In Fig. 11, we compare the reconstructed spectral curves with the original spectral curves of the three different kinds of materials. The spectra of pixel-(60, 60), pixel-(20, 20), and pixel-(90, 90) are selected for delegating B_1 , B_2 , and T , respectively. The first row of Fig. 11 shows the results of the \mathcal{X}_{Bg} reconstructed by one, two, and three PCs in SSRX. The remaining three rows of Fig. 11 are the results of the \mathcal{X}_{Bg} reconstructed by the TenB algorithm, with the spectral PC number changed in each column and with the spatial PC number changed in each row.

Fig. 11(a) shows that SSRX-1 has only reconstructed one kind of curve that corresponds to the most important background (B_1). In Fig. 11(b), two kinds of curves have been reconstructed by SSRX-2, which are the spectral curves of B_1 and B_2 . Moreover, some information of T has also been reconstructed (blue curve). This is because T 's spectrum is highly correlative with B_2 's spectrum, and the information of these two spectra may be contained in the same spectral PC. This phenomenon reflects that only using spectral PCs cannot separate two kinds of spectra with high correlation, which is one of the main shortcomings of the spectral-based method. Fig. 11(c) shows the well-reconstructed result of the three spectra by SSRX-3. Fig. 11(d)–(f) shows that the reconstructed curves do not change, although the spectral PC number changed. This is because the PC numbers of two spatial modes are set to one. In this case, only the most important material of \mathcal{X} can be reconstructed in \mathcal{X}_{Bg} . As a result, the shape of the green curve (indicates reconstructed B_2) is almost the same as that of the cyan curve (indicates original B_1), and the red and blue curves can be regarded as reconstruction error. In Fig. 11(g), although the spatial PC numbers are two, the spectral PC number is one. Hence, still only one kind of curve is well reconstructed. Analogously, Fig. 11(j) has also reconstructed one kind of curve (B_1) because the spectral PC number is one, too. Due to that fact that the spatial PC numbers are set to two, Fig. 11(h) and (i) shows that two kinds of curves are well reconstructed. Fig. 11(l) shows that all the three kinds of

materials are well reconstructed. This is because the three PC numbers are all selected as three, which is accordant with the real material number of \mathcal{X} . It is worth noting that Fig. 11 shows the reconstructed spectra in the background component of the HSI data.

From all the results recorded in Figs. 10 and 11, some conclusions may be drawn as follows: 1) The user-specified parameters (PC numbers) are more convenient for determining by the reconstruction-error-based method than by the traditional energy-cumulative method; 2) due to the background estimation being restricted by both the spectral and spatial PCs in the TenB algorithm, the TenB algorithm can separate the spectra with high correlation; and 3) the TenB algorithm is superior to the SSRX algorithm in background estimation.

b) Anomaly detection: Since the anomalies will be detected in \mathcal{X}_{An} , the characteristic of \mathcal{X}_{An} should be analyzed primarily. The signal-to-interference-plus-noise ratio (SINR) criterion is used to measure the spectral behavior of anomaly with the background, denoted as $\text{SINR} = T^T \Gamma^{-1} T$ [46], where T is the anomaly spectrum [pixel-(90, 90)] and Γ is the image covariance matrix. The anomaly is more prominent in the background when SINR is larger. The SINR results are reported in Table I. It is clear that the SINR of the data reconstructed by TenB-(2, 2, 1) is the largest. This phenomenon indicates that the TenB-(2, 2, 1) is the most proper for anomaly detection. Such conclusion could be further confirmed by the comparisons of the reconstructed curves of the three materials in \mathcal{X}_{An} , which are shown in Fig. 12. It illustrates the differences between the three materials. The spectrum of pixel-(90, 90) is more distinct than the other two spectra, and T is more easily to be detected. Fig. 12(g) has shown the most difference. It is the data reconstructed by TenB-(2, 2, 1).

Combining all the experiments mentioned earlier, some conclusions may be obtained: 1) If only considering the information preservation, SSRX-3 and TenB-(3, 3, 3) are both the best because they can well reconstruct all the materials' spectra in \mathcal{X} . Moreover, the PC numbers of the three modes are all 3, which reveals the actual material number contained in the original data. 2) If the aim is both background estimation and anomaly detection, neither SSRX-3 nor TenB-(3, 3, 3) is appropriate, but the TenB-(2, 2, 1) is. This is because, in the \mathcal{X}_{Bg} of TenB-(3, 3, 3), not only the background information is reconstructed but also the anomaly information. In this condition, little or even no anomaly information remained in \mathcal{X}_{An} . Therefore, the SINR is worse, and the detection result of \mathcal{X}_{An} is bad. On the

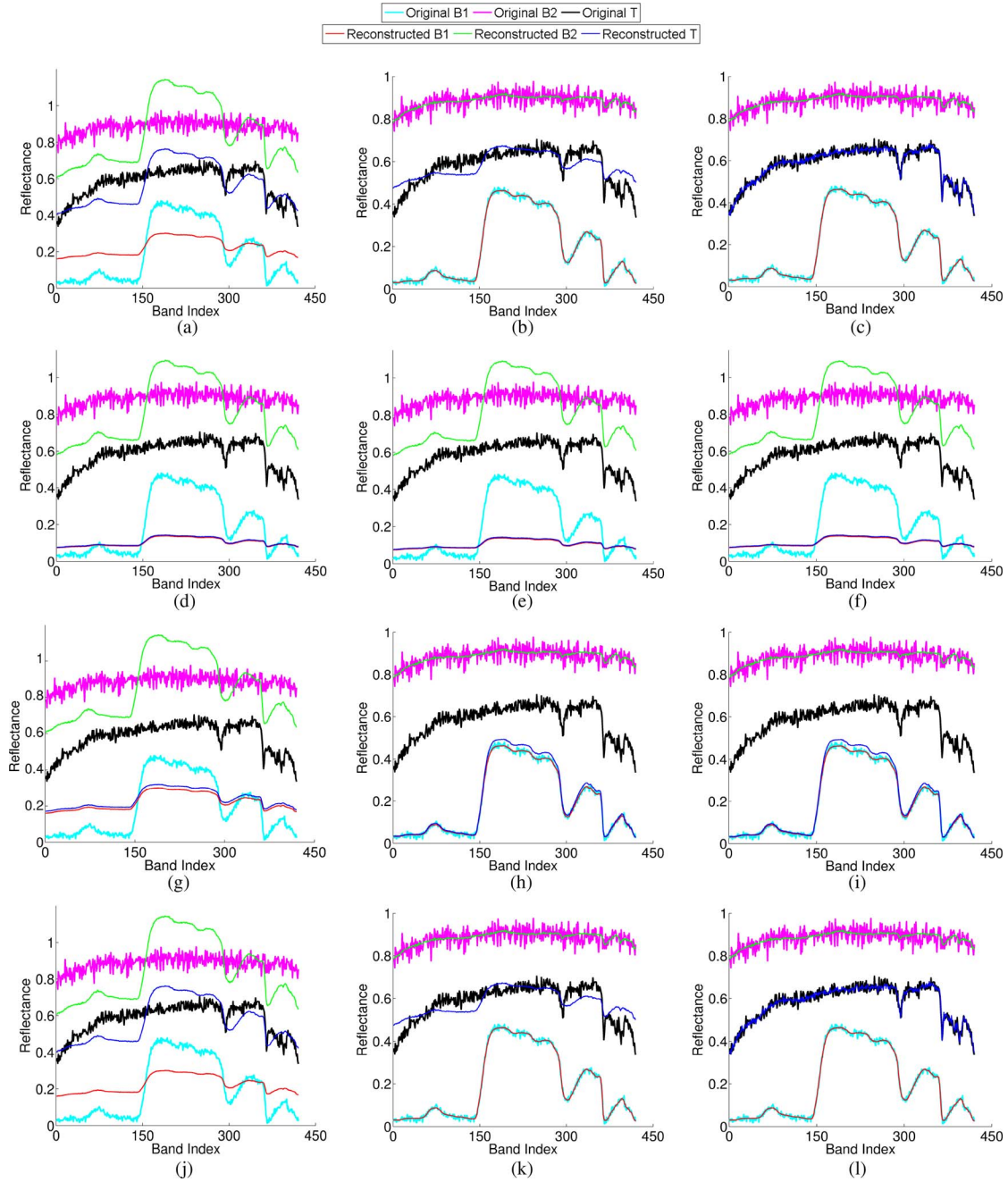


Fig. 11. Comparisons between reconstructed spectral curves and original curves of the three different kinds of materials in \mathcal{X}_{B_g} . The first row shows the results of SSRX with one, two, and three PCs to reconstruct, denoted as SSRX-1 for (a), SSRX-2 for (b), and SSRX-3 for (c). The second row shows the results of TenB with one, two, and three PCs along the spectral mode to reconstruct (the PC number along the two spatial modes is one), denoted as TenB-(1, 1, 1) for (d), TenB-(1, 1, 2) for (e), and TenB-(1, 1, 3) for (f). The remaining two rows are analogous to the second row with the spatial PC number changed, which are the results of TenB-(2, 2, 1) for (g), TenB-(2, 2, 2) for (h), TenB-(2, 2, 3) for (i), TenB-(3, 3, 1) for (j), TenB-(3, 3, 2) for (k), and TenB-(3, 3, 3) for (l).

TABLE I
SINR COMPARISONS FOR SIMULATED HSI DATA

	RXD	SSRX			TenB								
		1	2	3	(1,1,1)	(1,1,2)	(1,1,3)	(2,2,1)	(2,2,2)	(2,2,3)	(3,3,1)	(3,3,2)	(3,3,3)
SINR	39.93	39.92	38.83	27.25	40.00	41.60	28.33	44.50	38.88	29.02	-57.45	-57.63	-57.79

other hand, in the \mathcal{X}_{B_g} of TenB-(2, 2, 1), only the background information is well reconstructed, and the anomaly information is retained in \mathcal{X}_{A_n} . In this case, \mathcal{X}_{A_n} is assumed to be modeled as the anomaly signatures with residual error (assumed to be

a Gaussian noise). As a result, anomalies may be viewed as lying in a unimodal Gaussian background. Fig. 13 shows the histograms of the first band of the original data, \mathcal{X}_{A_n} reconstructed by SSRX-1 and \mathcal{X}_{A_n} reconstructed by TenB-(2, 2, 1),

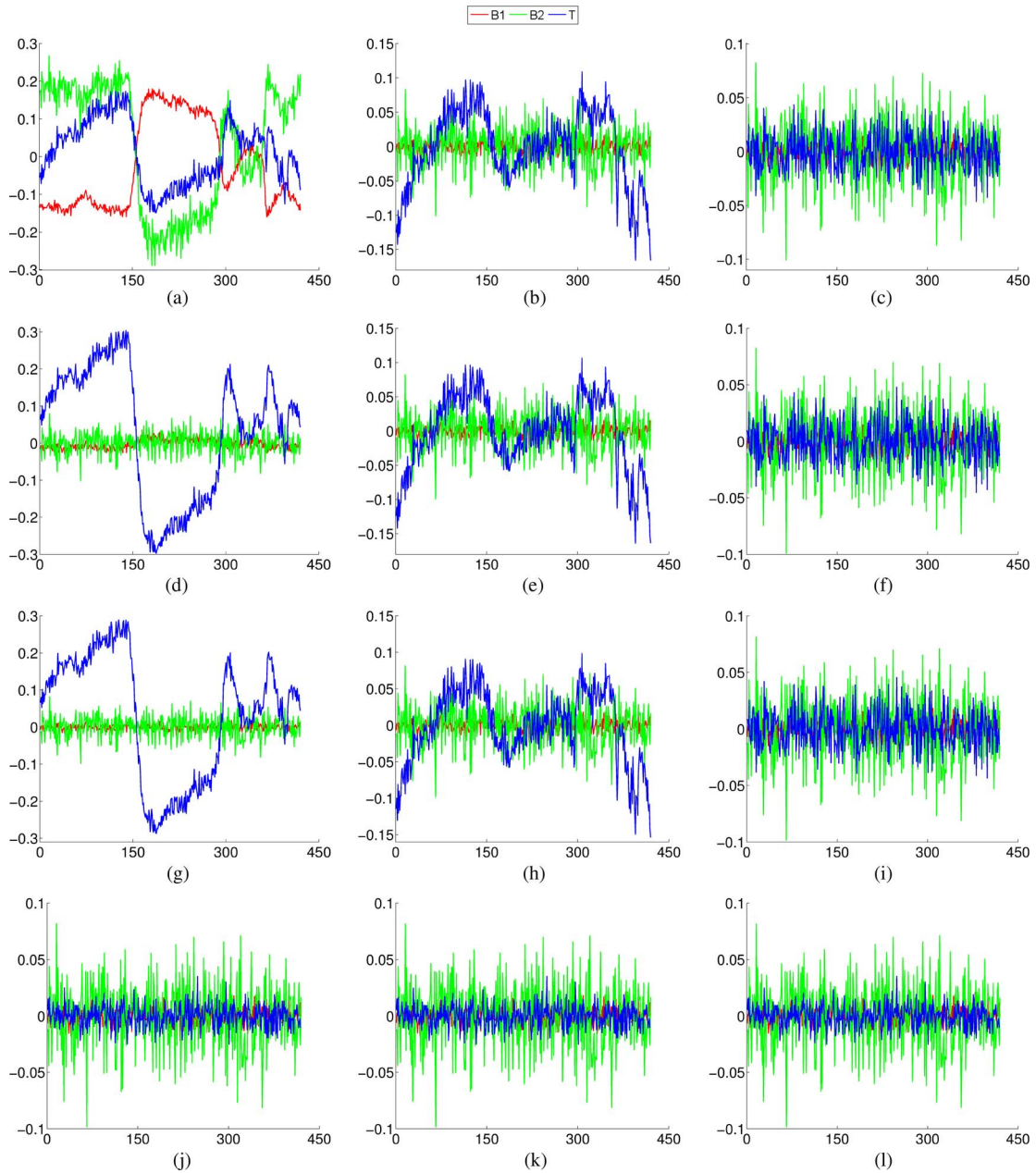


Fig. 12. Reconstructed spectral curves in \mathcal{X}_{An} . The first row shows the results of SSRX with one, two, and three PCs to reconstruct, denoted as SSRX-1 for (a), SSRX-2 for (b), and SSRX-3 for (c). The second row shows the results of TenB with one, two, and three PCs along the spectral mode to reconstruct (the PC number along the two spatial modes is one), denoted as TenB-(1, 1, 1) for (d), TenB-(1, 1, 2) for (e), and TenB-(1, 1, 3) for (f). The remaining two rows are analogical to the second row with the spatial PC number changed, which are the results of TenB-(2, 2, 1) for (g), TenB-(2, 2, 2) for (h), TenB-(2, 2, 3) for (i), TenB-(3, 3, 1) for (j), TenB-(3, 3, 2) for (k), and TenB-(3, 3, 3) for (l).

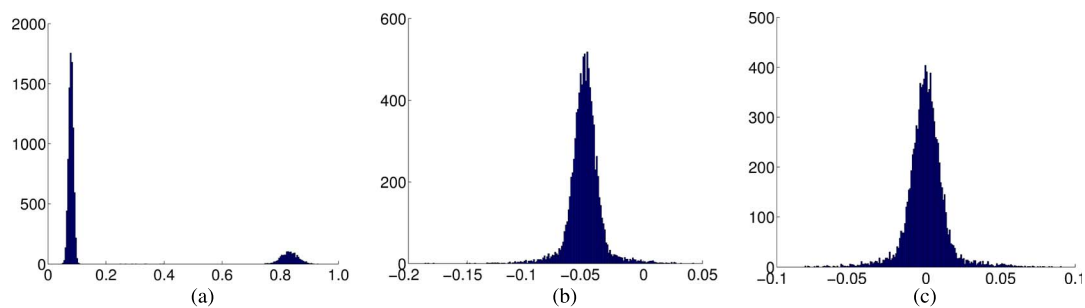


Fig. 13. Histograms of the first band of different data sets. (a) Original data. (b) \mathcal{X}_{An} reconstructed by SSRX-1. (c) \mathcal{X}_{An} reconstructed by TenB-(2, 2, 1).

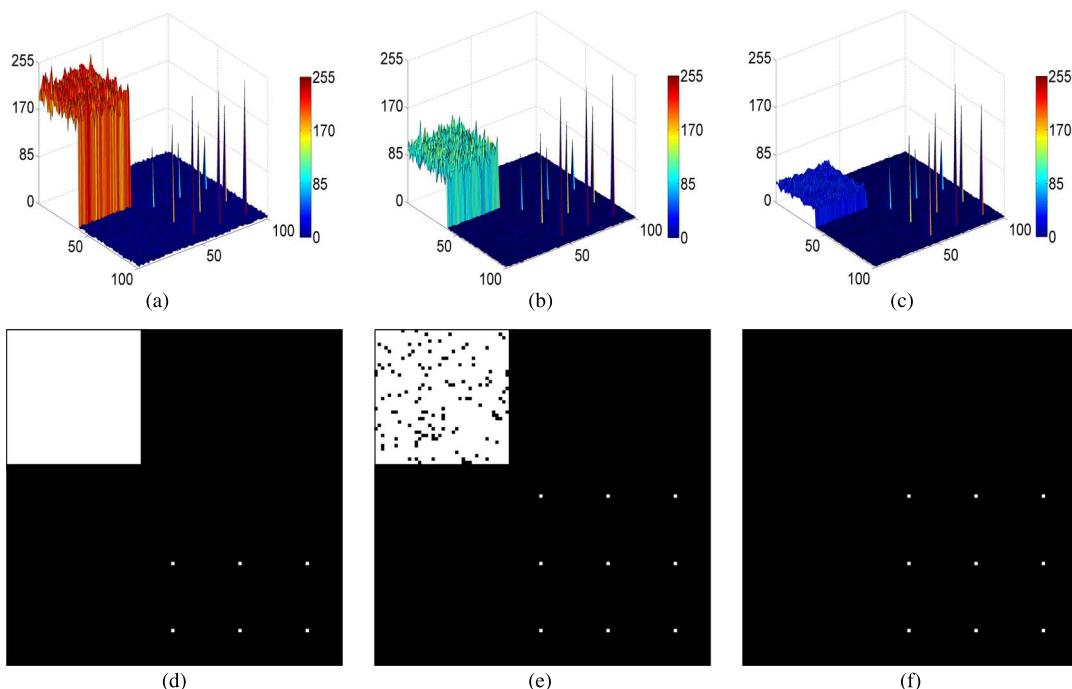


Fig. 14. Detection results for the simulated data. (a) Three-dimensional plot of RXD. (b) Three-dimensional plot of SSRX-1. (c) Three-dimensional plot of TenB-(2, 2, 1). (d) Binary image of (a) under the adaptive threshold. (e) Binary image of (b) under the adaptive threshold. (f) Binary image of (c) under the adaptive threshold.

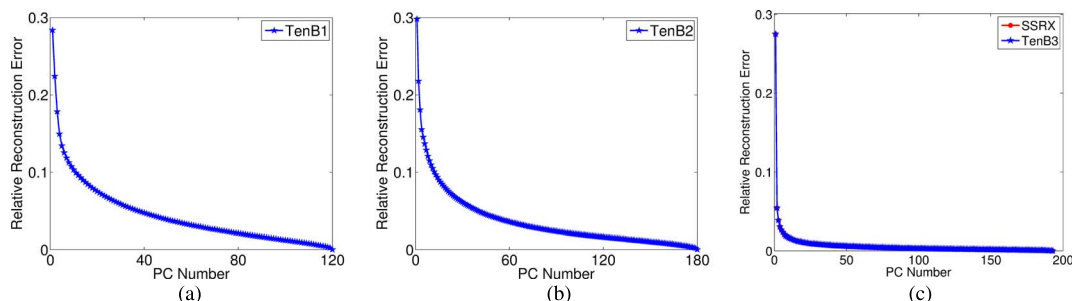


Fig. 15. Relative reconstruction error curves of ROI-1. (a) TenB method along the first mode. (b) TenB method along the second mode. (c) TenB method along the third mode and SSRX method.

respectively. It is clearly that the original data are a multimodal distribution [see Fig. 13(a)] while the remaining data after background elimination are more likely to be a unimodal Gaussian distribution [see Fig. 13(b) and (c)]. TenB-(2, 2, 1) has shown a better Gaussian characteristic than SSRX-1 with the mean of 0. The CFAR test is considered as a good strategy for anomaly detection in this type of data.

Basing on the aforementioned analyses, a CFAR test is implemented to detect the anomalies from \mathcal{X}_{An} . The detection results are shown in Fig. 14. From such figure, we can see that, compared to the background, the detection energy of the anomaly increases when background is eliminated in advance, particularly in the TenB-(2, 2, 1) method. When comparing the binary detection results, an important phenomenon is that only the nine real anomalous targets have been detected in TenB-(2, 2, 1) [see Fig. 14(f)]. On the other hand, in RXD, the whole pixels of $B2$ are detected as the anomalies, but the low-abundance-fraction anomalous targets (the first row) have not been detected [see Fig. 14(d)]; in SSRX-1, although all the nine real anomalous targets have been detected, some pixels

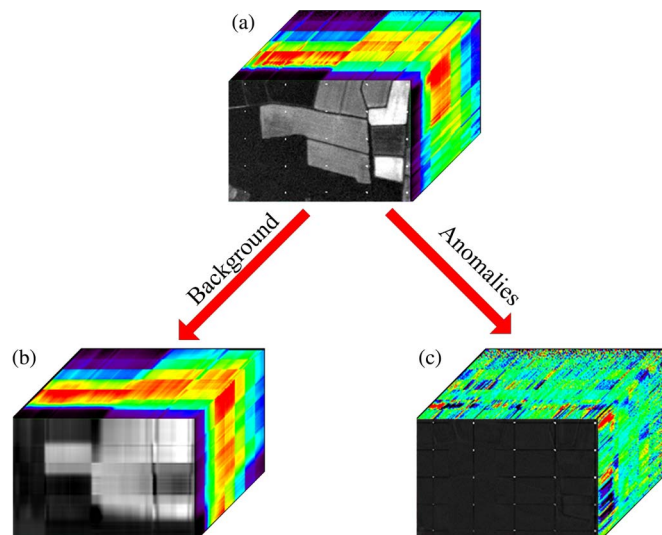


Fig. 16. Tensor reconstruction results of ROI-1 by TenB-(4, 4, 3). (a) Three-dimensional data cube of the original ROI-1. (b) Three-dimensional data cube of the \mathcal{X}_{Bg} . (c) Three-dimensional data cube of the \mathcal{X}_{An} .

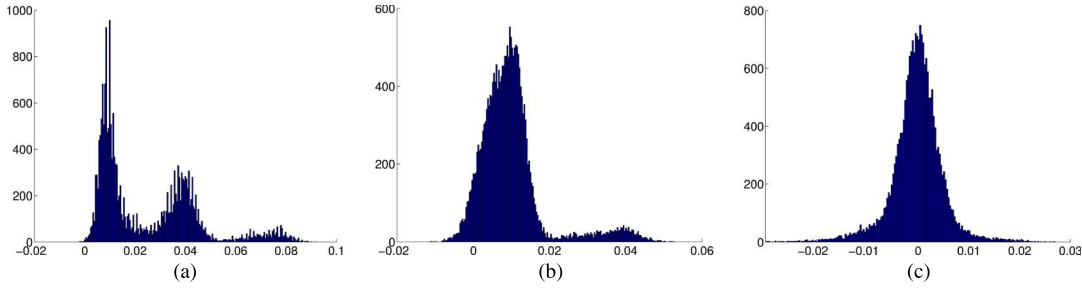


Fig. 17. Histograms of the first band of different data sets. (a) Original data. (b) \mathcal{X}_{An} reconstructed by SSRX-3 for ROI-1. (c) \mathcal{X}_{An} reconstructed by TenB-(4, 4, 3) for ROI-1.

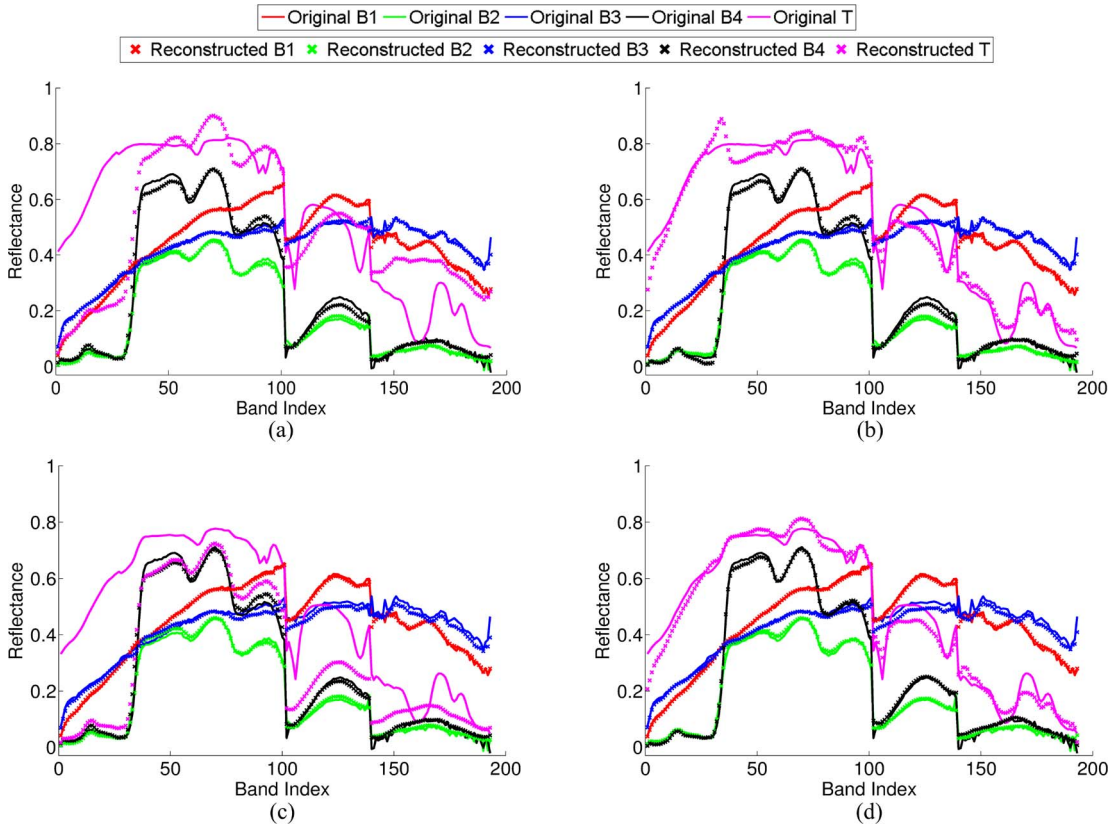


Fig. 18. Comparisons between reconstructed spectral curves and original curves of the backgrounds and target in X_{Bg} . The first row shows the results of SSRX with three and four PCs to reconstruct, denoted as SSRX-3 for (a) and SSRX-4 for (b). The second row shows the results of TenB, denoted as TenB-(4, 4, 3) for (c) and TenB-(5, 5, 4) for (d).

of $B2$ are also detected as the anomalies [see Fig. 14(e)]. This phenomenon has proved that, when detecting the anomalies, the RXD and SSRX-1 methods only exploit the spectral anomaly but do not consider the spatial anomaly. As mentioned earlier, an anomaly possesses spectral anomaly and spatial anomaly simultaneously. Therefore, in this example, only T is considered as actual anomalous targets, but not $B2$, notwithstanding that the difference between the spectra of $B2$ and $B1$ is larger than that between the spectra of T and $B1$. $B2$ only owns spectral anomaly. In fact, an anomaly may not contain such large number of pixels. Therefore, $B2$ is more likely to be a kind of background than to be an anomaly. The detection results have shown the distinction between the spectral-based anomaly detection method and the spectral-spatial anomaly detection method.

2) *Experiment 2—ROI-1*: In order to determine the PC number, like *Experiment 1*, we analyze the relative reconstruction error along different modes at first. The results are shown in Fig. 15. According to Fig. 15, the spectral PC number is set to two, and the two spatial PC numbers are set to four. As a result, SSRX-3 and TenB-(4, 4, 3) are considered for anomaly detection in the following content.

The tensor reconstruction results of ROI-1 according to the process of II-C are shown in Fig. 16. As can be seen, two subtensors are obtained from the decomposition of the original data cube [see Fig. 16(a)], where \mathcal{X}_{Bg} provides the background scene with scarcely any anomalous signals [see Fig. 16(b)] and \mathcal{X}_{An} provides a scene with the prominence of the anomalies [see Fig. 16(c)]. Fig. 16 has proved that the TenB-(4, 4, 3) method can separate background information and anomaly

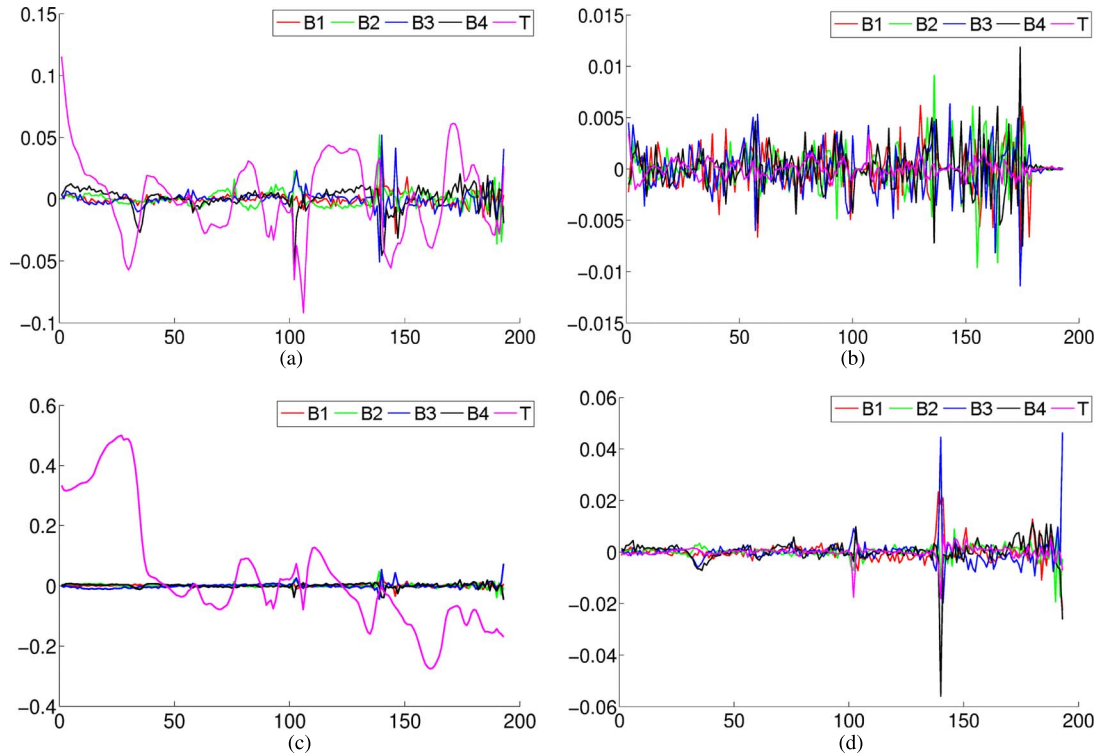


Fig. 19. Reconstructed spectral curves in \mathcal{X}_{An} . The first row shows the results of SSRX with three and four PCs to reconstruct, denoted as SSRX-3 for (a) and SSRX-4 for (b). The second row shows the results of TenB, denoted as TenB-(4, 4, 3) for (c) and TenB-(5, 5, 4) for (d).

information effectively. Furthermore, Fig. 17 has shown the Gaussian characteristic of different data sets. It is clear that the TenB-(4, 4, 3) method has got a most proximal unimodal Gaussian distribution like background.

Here, we also give the spectra reconstruction experimental analysis on ROI-1. In Fig. 18, we compare the reconstructed spectral curves with the original spectral curves of the backgrounds and target. If we list all the subfigures for the combination of parameters (spectral PC number and spatial PC number) like Fig. 11, each subfigure could be too small for reading. Therefore, we just list the two most important subfigures for SSRX and TenB, respectively. One subfigure delegates the most proper parameter for background spectra reconstruction only. Fig. 18(a) is for SSRX-3, and Fig. 18(c) is for TenB-(4, 4, 3). The other subfigure delegates the most proper parameter for the whole spectra (background and target) reconstruction. Fig. 18(b) is for SSRX-4, and Fig. 18(d) is for TenB-(5, 5, 4). Fig. 18(a) and (c) shows that SSRX-3 and TenB-(4,4,3) have well reconstructed the four backgrounds, while the target spectrum has not been reconstructed. Due to the fact that B_2 and B_4 are highly correlated in the spectral domain, setting the spectral PC number as three is enough for reconstructing the four backgrounds. By analogy, only four spectral PCs are needed for the whole spectra reconstruction.

The only difference in Fig. 18(a) and (c) is the reconstructed T . In Fig. 18(a), the shape of the reconstructed T is likely to be a mixed spectrum by the backgrounds, but its reflectance amplitude is close to the original T (larger than the backgrounds) in some band ranges. This phenomenon indicates that some information of T may be reconstructed in the \mathcal{X}_{Bg} of SSRX-3.

TABLE II
SINR COMPARISONS FOR ROI-1

	RXD	SSRX		TenB	
		4	5	(4,4,3)	(5,5,4)
SINR	29.94	30.05	13.15	38.72	16.67

On the other hand, in Fig. 18(c), the reconstructed T is almost the same as B_4 , meaning that hardly any information of T is contained in the \mathcal{X}_{Bg} of TenB-(4, 4, 3). Fig. 18(b) and (d) shows that B_1 , B_2 , B_3 , B_4 , and T are all well reconstructed. TenB-(5, 5, 4) obtains better reconstructed T than SSRX-4.

Fig. 19 shows the corresponding results of the reconstructed spectra in the \mathcal{X}_{An} . As shown in the figure, T is more prominent in Fig. 19(c) than in Fig. 19(a), meaning that T is more easily to be detected in the \mathcal{X}_{An} of TenB-(4, 4, 3). Such conclusion could be further confirmed by the comparisons of SINR listed in Table II. The SINR of TenB-(4, 4, 3) is the largest.

For illustrative purposes, Fig. 20 presents the anomaly detection results of the three considered algorithms applied to ROI-1. The results presented in Fig. 20(d)–(f) have been obtained by applying a segmentation with the threshold computed in (11) to the direct detection results, resulting in a set of binary images that can be used as an indication to evaluate the performance of the different compared algorithms. From Fig. 20, several conclusions may be obtained: 1) The TenB-(4, 4, 3) method outputs the best separability of background–anomaly; 2) TenB-(4, 4, 3) has detected all the anomalies in the image, while SSRX-3 and RXD have missed some low-abundance-fraction anomalous targets (RXD is worse); and 3) both SSRX-3 and

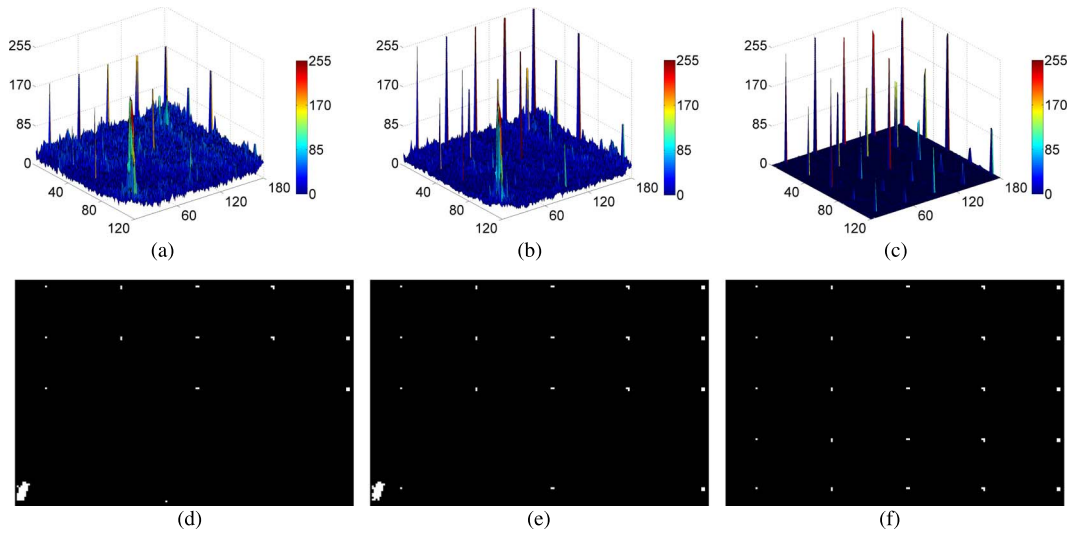


Fig. 20. Detection results for Hyperion data set (ROI-1). (a) Three-dimensional plot of RXD. (b) Three-dimensional plot of SSRX-3. (c) Three-dimensional plot of TenB-(4, 4, 3). (d) Binary image of (a) under the adaptive threshold. (e) Binary image of (b) under the adaptive threshold. (f) Binary image of (c) under the adaptive threshold.

RXD have generated several false alarms, but none in TenB-(4, 4, 3). The main reasons for these phenomena may be twofold: 1) TenB-(4, 4, 3) eliminates the background information in both the spectral and spatial domains before detecting, which may suppress more energy of background than SSRX-3 and RXD. The anomalies left in the remaining data are considered as spectral-spatial anomalies lying in a unimodal Gaussian background. As a result, they can be detected more easily. 2) The main false alarm pixels in the results of SSRX-3 and RXD are from the interferential object in the left-bottom corner. Although this object's spectrum is different from the background spectra, it owns about 50 pixels. In fact, it is too large to be an anomalous target. In other words, the interferential object only possesses a spectral-anomaly characteristic but not the spatial-anomaly characteristic. SSRX-3 and RXD are the right algorithms that only exploit the spectral anomaly, so the interferential object has been detected as anomaly. On the other hand, TenB-(4, 4, 3) detects the object with both of the two anomaly characteristics, so the interferential object has not been detected as anomaly.

A quantitative comparison is reported in Fig. 21 with ROC curves and the AUC values (listed in the brackets). A superior detector would lie nearer the top left and own a larger AUC. The ROC curves in Fig. 21 reveal that most of the methods perform well for ROI-1, except for the RXD. Those detectors are not particularly distinguishable at the low value range of detection probability.

This phenomenon indicates that those methods perform similarly when fewer anomalous targets are separated from the background. Since the most separable anomalous targets are the ones with high abundance fraction, all of the methods are able to detect these ones easily. With higher detection probability, which suggests that the more difficult anomalous targets (with low abundance fraction) are separated, the ROC curves appear different. At this time, the false alarm rate can be used as an indicator for the separation ability of the different detection

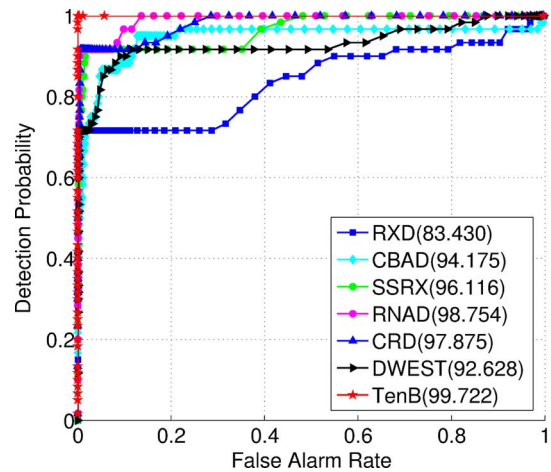


Fig. 21. ROC curves for Hyperion data set (ROI-1).

methods. TenB lies nearer the upper left in the axis space than the others, and it performs best at most ranges, which indicates that the method detects more difficult anomalous targets, with better separability from the backgrounds. Therefore, the detection performance of TenB is much superior to that of the compared methods for the ROI-1 scene. Such conclusion could be further verified by the AUC values, where TenB provides the highest AUC value.

3) *Experiment 3—ROI-2*: Likewise, for ROI-2, we first analyze the relative reconstruction error for determining the PC number along different modes. According to Fig. 22, we determine the spectral PC number as two and both of the two spatial PC numbers as four. As a result, SSRX-2 and TenB-(4, 4, 2) are considered for anomaly detection in the following experiments.

The tensor reconstruction results of ROI-2 are shown in Fig. 23. The same phenomenon observed in this experiment is that the original HSI data cube may be divided into two

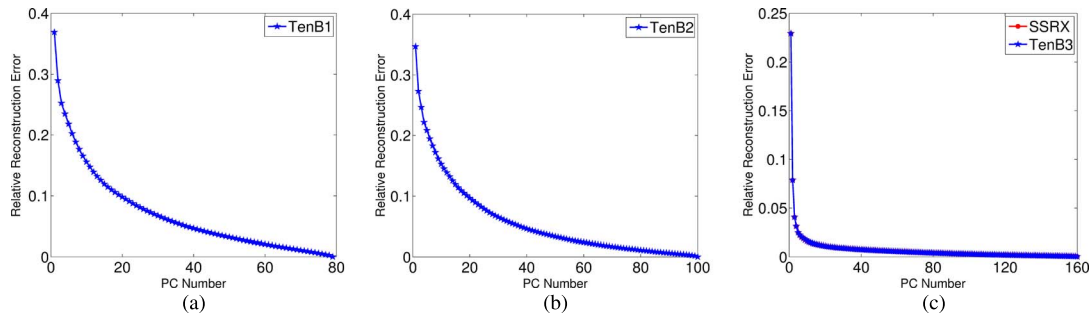


Fig. 22. Relative reconstruction error curves of ROI-2. (a) TenB method along the first mode. (b) TenB method along the second mode. (c) TenB method along the third mode and SSRX method.

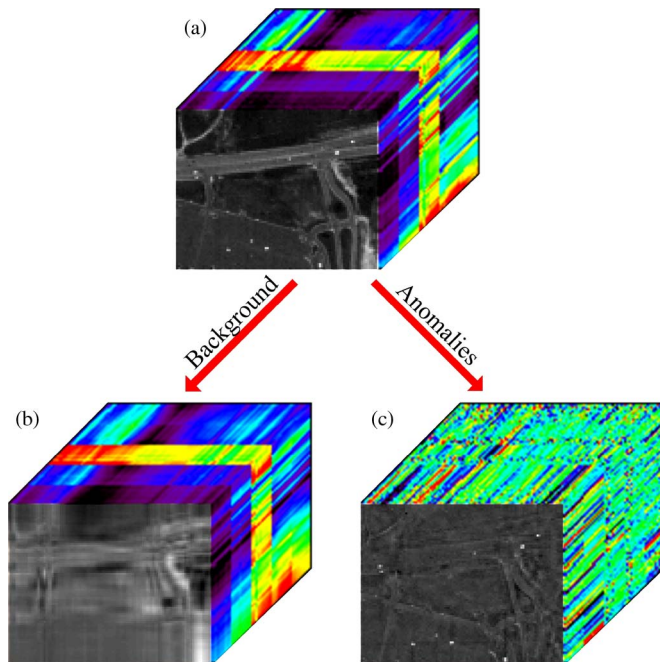


Fig. 23. Tensor reconstruction results of ROI-2. (a) Three-dimensional data cube of ROI-2. (b) Three-dimensional data cube of the \mathcal{X}_{Bg} . (c) Three-dimensional data cube of the \mathcal{X}_{An} .

subtensors in which one indicates the main background information (denoted as \mathcal{X}_{Bg}) and the other indicates the anomalous part (denoted as \mathcal{X}_{An}). From Fig. 23, we can see clearly that little anomalous information is contained in \mathcal{X}_{Bg} , while anomalies are salient in a single background (Gaussian-like distribution) in \mathcal{X}_{An} . This phenomenon illustrates that TenB-(4, 4, 2) has separated background and anomalies effectively. Furthermore, Fig. 24 has shown the Gaussian characteristic of different data sets. It has verified that the TenB-(4,4,2) method has got a most proximal unimodal Gaussian distribution like background.

Detection results obtained after applying the three considered algorithms to ROI-2 are reported in Fig. 25. The real anomalies having been detected are labeled in red rings. In general, we can observe that TenB-(4, 4, 2) has detected the most targets with the fewest false alarms comparing to the RXD and SSRX-2 algorithms [see Fig. 25(d)–(f)]. From the results, we may draw some conclusions: 1) Due to the complexity of the background,

the anomalies may be enshrouded by background information. As a result, detection on the original data [see Fig. 25(d)] may miss some anomalies. On the other hand, after background elimination, this influence may be mitigated. Consequently, the detection probability may be increased [see Fig. 25(e) and (f)]. This phenomenon proves that background elimination is propitious to anomaly detection. 2) The TenB-(4, 4, 2) method shows superiority over SSRX-2 in anomaly detection. SSRX-2 only eliminates background information in the spectral domain. In this case, if the spectra of anomalous targets correlate with the background spectra, some information of anomalous targets may be weakened when eliminating background. As a result, the detection probability may be reduced. On the other hand, the TenB-(4, 4, 2) method eliminates background information in both the spectral and spatial domains. Anomalies are not only spectrally different from background but also spatially distinct. In this case, even if the spectra of anomalous targets correlate with the background spectra, the spatial distribution differences between them still exist in most cases. Therefore, background and anomaly can be distinguished in the spectral–spatial domain, and they can be separated effectively. Furthermore, anomalies can be easily detected in the background-free data. The TenB-(4, 4, 2) algorithm has made a noticeable improvement with regard to the two contrastive algorithms in this particular experiment.

The detection performances of the considered methods are quantitatively compared by the ROC curves and the AUC values reported in Fig. 26. TenB achieves a 100% detection probability at a comparatively low false alarm rate and gives the highest AUC value. Therefore, we may conclude that TenB is promising for detecting the anomalous targets from ROI-2.

4) *Experiment 4—ROI-3*: For ROI-3, we first analyze the relative reconstruction error for determining the PC number along different modes. As shown in Fig. 27, we determine the spectral PC number as two and both of the two spatial PC numbers as five. As a result, SSRX-2 and TenB-(5, 5, 2) are considered for anomaly detection in the following experiments.

Then, the detection performances of those methods are analyzed by the ROC curves reported in Fig. 28 and the AUC values listed in the brackets. This time, TenB is better at detecting the more difficult anomalous targets than its counterparts. The superior detection performance could be further confirmed by the AUC values.

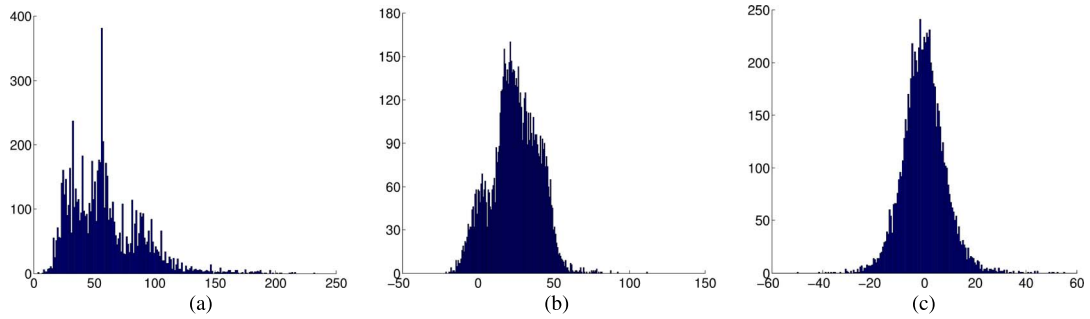


Fig. 24. Histograms of the first band of different data sets. (a) Original data set. (b) \mathcal{X}_{An} reconstructed by SSRX-2 for ROI-2. (c) \mathcal{X}_{An} reconstructed by TenB-(4, 4, 2) for ROI-2.

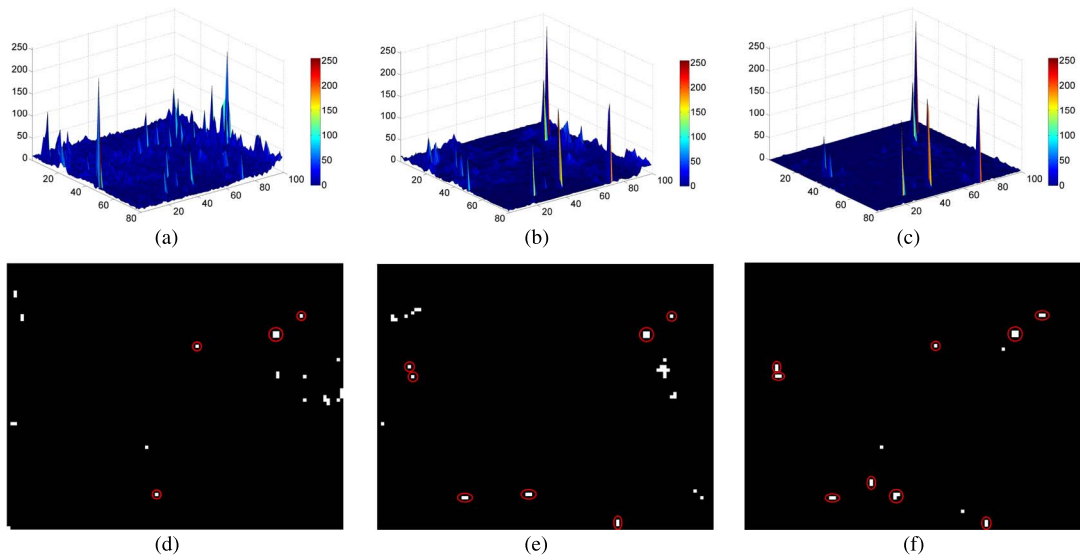


Fig. 25. Detection results for HYDICE data set. (a) Three-dimensional plot of RXD. (b) Three-dimensional plot of SSRX-2. (c) Three-dimensional plot of TenB-(4, 4, 2). (d) Binary image of (a) under the adaptive threshold. (e) Binary image of (b) under the adaptive threshold. (f) Binary image of (c) under the adaptive threshold.

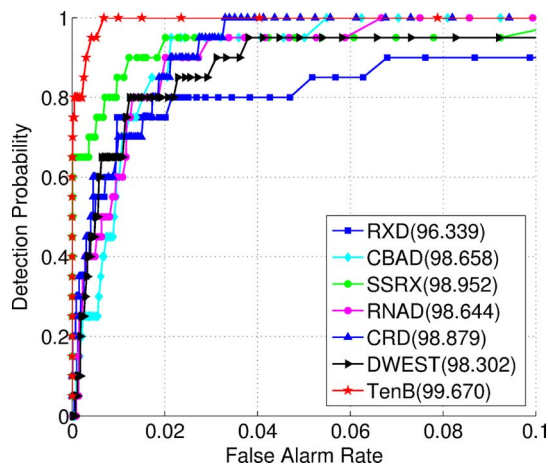


Fig. 26. ROC curves for HYDICE data set (ROI-2).

Finally, the computation costs of all of the aforementioned methods are also compared. The detailed results are presented in Table III. Specifically, the A, B, and C (following TenB)

correspond to the computation costs of each step in TenB. The algorithms are tested on a computer with an Intel Core i7-2600 CPU at 3.40 GHz and 4.0-GB RAM.

IV. CONCLUSION

In this paper, an anomaly detection algorithm based on tensor decomposition has been developed. The proposed algorithm is designed for detecting the targets with both spectral-anomaly and spatial-anomaly characteristics. Experiments on four HSI data sets have confirmed the efficiency of our method. It is demonstrated that the proposed TenB algorithm provides superior detection performance with better detection probability and less false alarm rate over the compared anomaly detection methods. However, the determination of three PC numbers (K_1 , K_2 , and K_3) still needs further studying, which will be the focus of our future work.

Moreover, the Tucker decomposition treats the three modes of HSI data equivalently. While the two spatial modes are highly correlative, they are radically different from the spectral mode. Hence, for HSI data processing, a new variation of the

TABLE III
COMPUTATION COST COMPARISON OF THE ALGORITHMS FOR THE THREE HSI DATA

HSI data	The algorithms						
	RXD	CBAD	SSRX	RNAD	CRD	DWEST	TenB(A+B+C)
ROI-1	0.4738	9.4280	0.5347	19.507	51.640	326.087	2.5826(1.9618+0.3161+0.3047)
ROI-2	0.1422	2.5379	0.3118	4.6950	17.039	90.658	0.9639(0.7418+0.1256+0.0965)
ROI-3	0.1034	0.8748	0.1932	2.0220	9.9979	49.731	0.7389(0.5952+0.0655+0.0782)

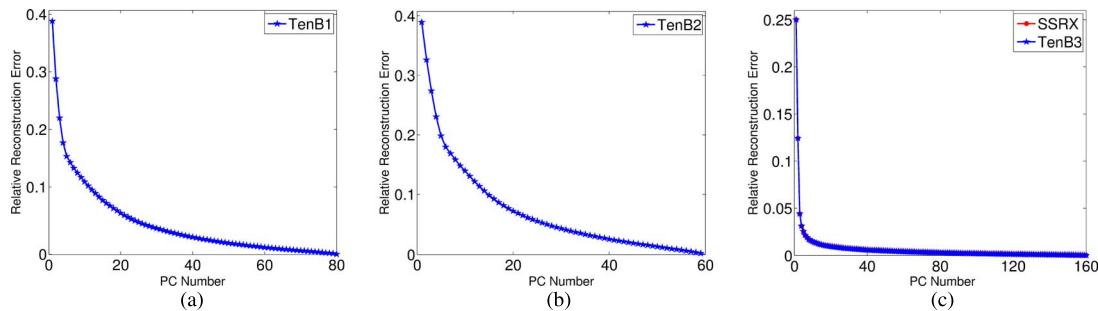


Fig. 27. Relative reconstruction error curves of ROI-3. (a) TenB method along the first mode. (b) TenB method along the second mode. (c) TenB method along the third mode and SSRX method.

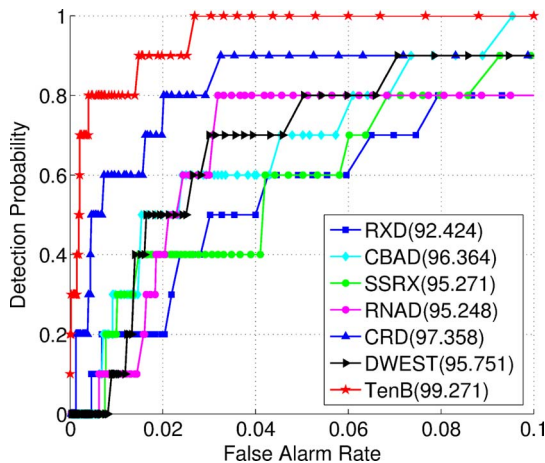


Fig. 28. ROC curves for ROI-3.

Tucker decomposition should be designed, in which the 3-D structured data are considered to be decomposed into a 1-D spectral feature and a 2-D spatial feature. This may preserve the 2-D spatial correlations in each feature. It will be another focus of our future work.

REFERENCES

[1] M. T. Eismann, A. Stocker, and N. M. Nasrabadi, "Automated hyperspectral cueing for civilian search and rescue," *Proc. IEEE*, vol. 97, no. 6, pp. 1031–1055, Jun. 2009.

[2] D. W. J. Stein, S. G. Beaven, L. E. Hoff, E. M. Winter, A. P. Schaum, and A. D. Stocker, "Anomaly detection from hyperspectral imagery," *IEEE Signal Process. Mag.*, vol. 19, no. 1, pp. 58–69, Jan. 2002.

[3] N. M. Nasrabadi, "Hyperspectral target detection: An overview of current and future challenges," *IEEE Signal Process. Mag.*, vol. 31, no. 1, pp. 34–44, Jan. 2014.

[4] D. Manolakis, E. Truslow, M. Pieper, T. Cooley, and M. Brueggeman, "Detection algorithms in hyperspectral imaging systems: An overview of practical algorithms," *IEEE Signal Process. Mag.*, vol. 31, no. 1, pp. 24–33, Jan. 2014.

[5] S. Matteoli, M. Diani, and G. Corsini, "A tutorial overview of anomaly detection in hyperspectral images," *IEEE Aerosp. Electron. Syst. Mag.*, vol. 25, no. 7, pp. 5–28, Jul. 2010.

[6] I. S. Reed and X. Yu, "Adaptive multiple-band CFAR detection of an optical pattern with unknown spectral distribution," *IEEE Trans. Acoust., Speech, Signal Process.*, vol. 38, no. 10, pp. 1760–1770, Oct. 1990.

[7] M. J. Carlotte, "A cluster-based approach for detecting man-made objects and changes in imagery," *IEEE Trans. Geosci. Remote Sens.*, vol. 43, no. 2, pp. 374–387, Feb. 2005.

[8] S. Catterall, "Anomaly detection based on the statistics of hyperspectral imagery," in *Proc. SPIE Conf. Imagery Spectroscopy X*, 2004, vol. 5546, pp. 171–178.

[9] D. B. Marden and D. Manolakis, "Using elliptically contoured distributions to model hyperspectral imaging data," in *Proc. SPIE Algorithms Technol. Multispectr., Hyperspectr., Ultraspectr. Imagery X*, 2004, vol. 5425, pp. 558–572.

[10] A. Schaum, "Advanced hyperspectral detection based on elliptically contoured distribution models and operator feedback," in *Proc. IEEE AIRP*, 2009, pp. 1–5.

[11] J. Theiler, "Ellipsoid-simplex hybrid for hyperspectral anomaly detection," in *Proc. 3rd IEEE WHISPERS*, 2011, pp. 1–4.

[12] N. E. Billor, A. S. Hadib, and P. F. Velleman, "BACON: Blocked adaptive computationally efficient outlier nominators," *Comput. Statist. Data Anal.*, vol. 34, pp. 279–298, 2000.

[13] S. Matteoli, M. Diani, and G. Corsini, "Improved estimation of local background covariance matrix for anomaly detection in hyperspectral images," *Opt. Eng.*, vol. 49, no. 4, 2010, Art. no. 046201.

[14] B. Du and L. Zhang, "Random-selection-based anomaly detector for hyperspectral imagery," *IEEE Trans. Geosci. Remote Sens.*, vol. 49, no. 5, pp. 1578–1589, May 2011.

[15] R. Zhao, B. Du and L. Zhang, "A robust nonlinear hyperspectral anomaly detection approach," *IEEE J. Sel. Topics Appl. Earth Observ. Remote Sens.*, vol. 7, no. 4, pp. 1227–1234, Apr. 2014.

[16] Q. Guo, B. Zhang, Q. Ran, L. Gao, J. Li, and A. Plaza, "Weighted-RXD and linear filter-based RXD: Improving background statistics estimation for anomaly detection in hyperspectral imagery," *IEEE J. Sel. Topics Appl. Earth Observ. Remote Sens.*, vol. 7, no. 6, pp. 2351–2366, Jun. 2014.

[17] B. Du and L. Zhang, "A discriminative metric learning based anomaly detection method," *IEEE Trans. Geosci. Remote Sens.*, vol. 52, no. 11, pp. 6844–6857, Nov. 2014.

[18] K. I. Ranney and M. Soumekh, "Hyperspectral anomaly detection within the signal subspace," *IEEE Trans. Geosci. Remote Sens.*, vol. 3, no. 3, pp. 312–316, Jul. 2006.

[19] Y. Chen, N. Nasrabadi, and T. Tran, "Sparse representation for target detection in hyperspectral imagery," *IEEE J. Sel. Topics Signal Process.*, vol. 5, no. 3, pp. 629–640, Mar. 2011.

[20] Y. Chen, N. Nasrabadi, and T. Tran, "Simultaneous joint sparsity model for target detection in hyperspectral imagery," *IEEE Trans. Geosci. Remote Sens. Lett.*, vol. 8, no. 4, pp. 676–680, Apr. 2011.

[21] W. Li and Q. Du, "Collaborative representation for hyperspectral anomaly detection," *IEEE Trans. Geosci. Remote Sens.*, vol. 53, no. 3, pp. 1463–1474, Mar. 2015.

- [22] D. Borghys, I. Kasenb, and V. Achard, "Comparative evaluation of hyperspectral anomaly detectors in different types of background," in *Proc. SPIE Algorithms Technol. Multispectr., Hyperspectr., Ultraspectr. Imagery XVIII*, 2012, pp. 1–12.
- [23] H. Kwon, S. Z. Der, and N. M. Nasrabadi, "Adaptive anomaly detection using subspace separation for hyperspectral imagery," *Opt. Eng.*, vol. 42, no. 11, pp. 3342–3351, Nov. 2003.
- [24] W. Liu and C.-I. Chang, "Multiple-window anomaly detection for hyperspectral imagery," *IEEE J. Sel. Topics Signal Process.*, vol. 6, no. 2, pp. 644–658, Apr. 2013.
- [25] L. Zhang, L. Zhang, D. Tao, and X. Huang, "Tensor discriminative locality alignment for hyperspectral image spectral-spatial feature extraction," *IEEE Trans. Geosci. Remote Sens. Lett.*, vol. 51, no. 1, pp. 242–256, Jan. 2013.
- [26] L. Zhang, L. Zhang, D. Tao, X. Huang, and B. Du, "Compression of hyperspectral remote sensing images by tensor approach," *Neurocomputing*, vol. 147, no. 5, pp. 358–363, Jan. 2015.
- [27] T. Lin and S. Bourennane, "Survey of hyperspectral image denoising methods based on tensor decompositions," *EURASIP J. Adv. Signal Process.*, vol. 2013, pp. 1–11, Dec. 2013.
- [28] N. Renard, S. Bourennane, and J. Blanc-Talon, "Robust target detection by spatial/spectral restoration based on tensor modeling," *IEEE Trans. Geosci. Remote Sens.*, vol. 46, no. 8, pp. 2407–2416, Aug. 2008.
- [29] S. Velasco-Forero and J. Angulo, "Classification of hyperspectral images by tensor modeling and additive morphological decomposition," *Pattern Recognit.*, vol. 46, pp. 566–577, 2013.
- [30] Z. Zhong *et al.*, "Discriminant tensor spectral-spatial feature extraction for hyperspectral image classification," *IEEE Trans. Geosci. Remote Sens. Lett.*, vol. 12, no. 5, pp. 1028–1032, May 2015.
- [31] Q. Zhang, H. Wang, R. J. Plemmons, and V. P. Pauca, "Tensor methods for hyperspectral data analysis: A space object material identification study," *J. Opt. Soc. Amer. A*, vol. 25, no. 12, pp. 3001–3012, Dec. 2008.
- [32] L. D. Lathauwer, *Signal Processing Based on Multilinear Algebra*. Leuven, Belgium: Katholieke Univ. Leuven, 1997.
- [33] T. G. Kolda and B. W. Bader, "Tensor decompositions and applications," *SIAM Rev.*, vol. 51, no. 3, pp. 455–500, Mar. 2009.
- [34] L. D. Lathauwer, B. D. Moor, and J. Vandewalle, "On the best rank-1 and rank- (R_1, R_2, \dots, R_n) approximation of higher-order tensors," *SIAM J. Matrix Anal. Appl.*, vol. 21, no. 4, pp. 1324–1342, Apr. 2001.
- [35] P. Kroonenberg, *Three-Mode Principal Component Analysis*. Leiden, The Netherlands: DSWO, 1983.
- [36] L. Lathauwer, B. D. Moor, and J. Vandewalle, "A multilinear singular value decomposition," *SIAM J. Matrix Anal. Appl.*, vol. 21, no. 4, pp. 1253–1278, Apr. 2000.
- [37] P. M. Kroonenberg and J. De Leeuw, "Principal component analysis of three-mode data by means of alternating least squares algorithms," *Psychometrika*, vol. 45, no. 1, pp. 69–97, Mar. 1980.
- [38] A. Schaum, "Joint subspace detection of hyperspectral targets," in *Proc. IEEE Aerosp. Conf.*, 2004, vol. 3, pp. 1818–1824.
- [39] J. Y. Chen and I. S. Reed, "A detection algorithm for optical targets in clutter," *IEEE Trans. Aerosp. Electron. Syst.*, vol. AES-23, no. 1, pp. 46–59, Jan. 1987.
- [40] [Online]. Available: <http://speclab.cr.usgs.gov/spectral.lib06>
- [41] S. Khazai, S. Homayouni, A. Safari, and B. Mojaradi, "Anomaly detection in hyperspectral images based on an adaptive support vector method," *IEEE Geosci. Remote Sens. Lett.*, vol. 8, no. 7, pp. 646–650, Jul. 2011.
- [42] M. S. Stefanou and J. P. Kerekes, "A method for assessing spectral image utility," *IEEE Trans. Geosci. Remote Sens.*, vol. 47, no. 6, pp. 1698–1706, Jun. 2009.
- [43] S. M. Schweizer and J. M. F. Moura, "Efficient detection in hyperspectral imagery," *IEEE Trans. Image Process.*, vol. 10, no. 4, pp. 584–597, Apr. 2001.
- [44] L. Zhiyong, K. Gangyao, Y. Wenxian, and X. Qi, "Algorithm on small target detection based on principal component of hyperspectral imagery," *J. Infrared Millim. Waves*, vol. 23, no. 4, pp. 286–290, Aug. 2004.
- [45] J. Kerekes, "Receiver operating characteristic curve confidence intervals and regions," *IEEE Geosci. Remote Sens. Lett.*, vol. 5, no. 2, pp. 251–255, Apr. 2008.
- [46] D. Manolakis, D. Marden, and G. A. Shaw, "Hyperspectral image processing for automatic target detection applications," *Lincoln Lab. J.*, vol. 14, no. 1, pp. 79–116, Jan. 2003.



Xing Zhang received the B.S. degree in surveying and mapping engineering from the Wuhan University, Wuhan, China, in 2009 and the M.S. degree in photogrammetry and remote sensing from the National University of Defense Technology, Changsha, China, in 2011, where he is currently working toward the Ph.D. degree in the National Key Laboratory of Automatic Target Recognition.

His research interests include pattern recognition and hyperspectral image processing.



Gongjian Wen (M'16) received the B.S., M.S., and Ph.D. degrees from the National University of Defense Technology, Changsha, China, in 1994, 1997, and 2000, respectively.

Since 2009, he has been a Professor with the College of Electronic Science and Engineering, National University of Defense Technology, where he served as the head of the fourth department of the National Key Laboratory of Automatic Target Recognition. His research interests include image understanding, remote sensing, and target recognition.



Wei Dai received the B.S. degree in surveying and mapping engineering from the Wuhan University, Wuhan, China, in 2013 and the M.S. degree in information and communication engineering from the National University of Defense Technology, Changsha, China, in 2015.

His research interests include hyperspectral anomaly detection and dimensionality reduction.